Digital Quantum Simulation of a (1+1)D SU(2) Lattice Gauge Theory with Ion Qudits

Giuseppe Calajó[1,*] Giuseppe Magnifico[2,3,4] Claire Edmunds[5] Martin Ringbauer[5]
Simone Montangero[1,2,6] and Pietro Silvi[1,2,6]

[1]*Istituto Nazionale di Fisica Nucleare (INFN), Sezione di Padova, Padova I-35131, Italy*

[2]*Dipartimento di Fisica e Astronomia "G. Galilei," via Marzolo 8, Padova I-35131, Italy*

[3]*Dipartimento di Fisica, Università di Bari, Bari I-70126, Italy*

[4]*Istituto Nazionale di Fisica Nucleare (INFN), Sezione di Bari, Bari I-70125, Italy*

[5]*Universität Innsbruck, Institut für Experimentalphysik, Technikerstraße 25a, Innsbruck, Austria*

[6]*Padua Quantum Technologies Research Center, Universitá degli Studi di Padova, Padova I-35131, Italy*

We present a quantum simulation strategy for a (1+1)-dimensional SU(2) non-Abelian lattice gauge theory with dynamical matter, a hardcore-gluon Hamiltonian Yang-Mills, tailored to a six-level trapped-ion-qudit quantum processor, as recently experimentally realized [Nat. Phys. 18, 1053 (2022)]. We employ a qudit encoding fulfilling gauge invariance, an SU(2) Gauss's law. We discuss the experimental feasibility of generalized Mølmer-Sørensen gates used to efficiently simulate the dynamics. We illustrate how a shallow circuit with these resources is sufficient to implement scalable digital quantum simulation of the model. We also numerically show that this model, albeit simple, can dynamically manifest physically relevant properties specific to non-Abelian field theories, such as baryon excitations.

I. INTRODUCTION

Gauge theories are a fundamental theoretical framework in physics, playing an important role in many active areas of research spanning from high energies [1] to condensed matter [2] and quantum information science [3]. Their formulation on a lattice, known as lattice gauge theories, (LGTs) [4–6], is particularly suited to study nonperturbative effects. Monte Carlo techniques have been extremely successful over the years [7] in tackling various models, including quantum chromodynamics, but they are limited by the sign problem to certain physical regimes and struggle to capture the real-time evolution outside equilibrium [8]. In recent years, following the advances in quantum and quantum-inspired computation, alternative new possibilities to face these problems have emerged, based either on tensor-network numerical techniques [9–11] or on analog and digital quantum simulation [12–15], involving different experimental platforms such

as cold atoms [16–24], superconducting circuits [25–28] and trapped ions [29–33]. While with the numerical approach both Abelian [34–46] and non-Abelian [47–52] lattice-gauge-theory models have been theoretically studied, early demonstrations of quantum simulation of LGT largely focused on Abelian theories [30,32,53–58]. First attempts to tackle non-Abelian models have been proposed, relying ether on hybrid quantum computation schemes such as variational eigensolvers [27], while other quantum simulation encoding proposals are fairly limited in system size for realistic experimental platforms based on qubits [59–64].

One potential avenue to perform large-scale quantum computation relies on qudit-based quantum processors, which have been proposed in several platforms, such as Rydberg arrays [65,66], photonic circuits [67], and ultra-cold atomic mixtures [68]. An experimental breakthrough in this direction has been the demonstration of a universal seven-level optical-qudit quantum processor implemented on a chain of trapped $^{40}\mathrm{Ca}^+$ ions [69]. Using other ion species, the qudit dimension can be further extended as suggested by recent results with up to 13 levels [70]. These hardware developments have already stimulated interesting proposals [71–73] and experiments [74,75] for performing simulations of lattice gauge theories exploring this enlarged Hilbert space. However, a

proof-of-principle experimental demonstration of a scalable quantum simulation of the dynamics of non-Abelian LGTs is still lacking. Such demand is of fundamental importance not only to build new intuitions on not fully understood mechanisms of high-energy physics [1] but also to explore phenomena in condensed-matter models exhibiting non-Abelian topological order [76,77].

Here, we present a compact exotic fermion suborbital (rishon) representation for a truncated Yang-Mills SU(2) (1+1)-dimensional [(1+1)D] lattice gauge theory reduced to a six-dimensional local Hilbert space, embedding the gauge and fermionic degrees of freedom. This representation allows us to preserve the non-Abelian gauge symmetry, remove the fermionic character of matter (defermionization), and maintain the range of the gauge-matter interaction to nearest neighbors. This is in contrast with other approaches that rely either on the elimination of the gauge [31] or the matter [73] degree of freedom, which are not straightforwardly extendable to treat non-Abelian models, or on a fermionic qudit quantum processor [72,78] the proposal for which is currently limited to programmable Rydberg-array platforms. In this work, we present an experimentally feasible proposal based on a currently available ^{40}Ca$^+$ trapped-ion-qudit quantum processor [69,74]. In particular, we demonstrate how a digital quantum simulation of the model can be efficiently implemented by making use of generalized Mølmer-Sørensen (MS) gates realized by simultaneous driving of multiple transitions [79]. In this manner, we obtain a shallow circuit for each time step, enabling a feasible digital quantum simulation on current devices capable of distinguishing between bare-*meson* and -*baryon* production and thus signaling the non-Abelian nature of the model. Finally, we discuss the major challenges for the experimental realization of the proposal but we demonstrate that its implementation is compatible with current technologies.

This paper is structured as follows. In Sec. II, we introduce the (1+1)D SU(2) Yang-Mills lattice gauge model and derive the truncated qudit Hamiltonian defined on a local six-dimensional Hilbert space. In Sec. III, we present the strategy used to encode the model on a trapped-ion-qudit quantum processor and the generalized MS gates used in the quantum digital simulation. In Sec. IV, we show a few paradigmatic examples of the non-Abelian dynamics inherent in the model. In Sec. V, we present the strategy used to perform a quantum digital simulation of the model dynamics. In Sec. VI, we discuss the experimental feasibility of the proposal. Finally, in Sec. VII, we summarize our results and discuss future directions of research.

II. SU(2) LATTICE YANG-MILLS

We start by considering a Hamiltonian Yang-Mills lattice gauge model, with SU(2) color symmetry, in one spatial dimension, focusing on the low-energy regime. The
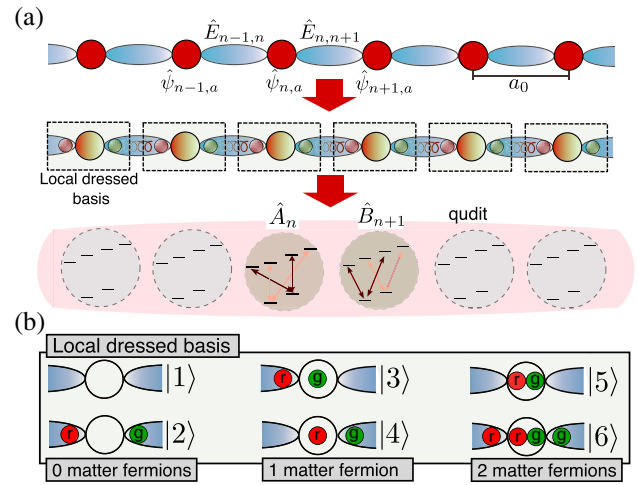

FIG. 1. A sketch of the model. (a) A (1+1)-dimensional [(1+1)D] Yang-Mills SU(2) lattice gauge model is encoded in a linear chain of trapped-ion qudits. The lattice gauge links (blue ovals) connecting the matter sites (red circles) are truncated to a five-dimensional Hilbert space. The mapping is then performed by exploiting the local dressed basis given in Eq. (5), obtained through the decomposition of the gauge links into a pair of rishons. (b) A pictorial representation of the local dressed basis given in Eq. (5). The red and green circles in the links represent the two colored rishons, while the ones in the sites represent the two colored matter fermions.

model illustrates a (flavorless) fermionic matter field coupled to an SU(2) gauge field, as depicted in Fig. 1(a). The matter field, representing quarks of bare mass m_0, is described by staggered fermions $\hat{\psi}_{na}$ [80], with two colors $a \in \{r, g\}$ (say, red and green), living on the lattice sites n and satisfying standard Dirac anticommutation rules $\{\hat{\psi}_{na}, \hat{\psi}^\dagger_{n'b}\} = \delta_{n,n'}\delta_{a,b}$. Conversely, the non-Abelian gauge field lives on the lattice bonds between sites n and $n+1$. Following the Kogut-Susskind formulation of gauge fields on a lattice [5], the system Hamiltonian reads

$$\hat{H}_0 = \frac{c\hbar}{2a_0} \sum_n \sum_{a,b=r,g} \left[-i\hat{\psi}^\dagger_{na} \hat{U}^{ab}_{n,n+1} \hat{\psi}_{n+1b} + \text{H.c.} \right]$$
$$+ m_0 c^2 \sum_{na} (-1)^n \hat{\psi}^\dagger_{na} \hat{\psi}_{na} + g_0^2 \frac{c\hbar}{2a_0} \sum_n \hat{E}^2_{n,n+1}, \quad (1)$$

where a_0 is the lattice spacing, $\hbar$ is the Planck constant, and c is the relativistic speed of free massless particles. The first two terms of Eq. (1) describe the lattice Hamiltonian of the covariant Dirac equation for massive quarks. It uses the staggered-mass term to create two sublattices, each representing a component of the two-spinor Dirac field, avoiding the doubling problem [80]. In this sense, quarks are staggered fermions on even sites, while antiquarks are staggered-fermion holes on odd sites.

The last term is the pure gauge Hamiltonian, which contains only an electric component $\hat{E}^2_{n,n+1}$, since there are no magnetic fields in one spatial dimension. The dimensionless coupling g_0^2 depends on the quark color charge q_c and on the lattice spacing a_0: in one spatial dimension, it scales as $g_0^2 = (q_c^2 a_0^2)/(c\hbar\epsilon_c)$, where ϵ_c is the vacuum color permittivity, assuming that the theory is super-renormalizable. The SU(2) electric field energy density is captured by the (dimensionless) quadratic Casimir operator $\hat{E}^2_{n,n+1} = |\hat{\mathbf{L}}_{n,n+1}|^2 = |\hat{\mathbf{R}}_{n,n+1}|^2$, where the algebra operators $\hat{L}^{(\nu)}_{n,n+1}$ and $\hat{R}^{(\nu)}_{n,n+1}$, with coordinates $\nu \in \{x,y,z\}$ are, respectively, the left and right group generators of the gauge transformation on each link. The gauge-field algebra is defined by the commutation rules

$$
\begin{aligned}
&\left[\hat{L}^{(\nu)}_{n,n+1}, \hat{R}^{(\nu')}_{n',n'+1}\right] = 0, \\
&\left[\hat{L}^{(\nu)}_{n,n+1}, \hat{L}^{(\nu')}_{n',n'+1}\right] = i\delta_{nn'}\epsilon^{\nu\nu'\nu''}\hat{L}^{(\nu'')}_{n,n+1}, \\
&\left[\hat{R}^{(\nu)}_{n,n+1}, \hat{R}^{(\nu')}_{n',n'+1}\right] = i\delta_{nn'}\epsilon^{\nu\nu'\nu''}\hat{R}^{(\nu'')}_{n,n+1}, \\
&\left[\hat{L}^{(\nu)}_{n,n+1}, \hat{U}^{ab}_{n',n'+1}\right] = -\delta_{nn'}\sum_c \frac{\sigma^{(\nu)}_{ac}}{2}\hat{U}^{cb}_{n,n+1}, \\
&\left[\hat{R}^{(\nu)}_{n,n+1}, \hat{U}^{ab}_{n',n'+1}\right] = \delta_{nn'}\sum_c \hat{U}^{ac}_{n,n+1}\frac{\sigma^{(\nu)}_{cb}}{2},
\end{aligned}
\tag{2}
$$

where $\epsilon^{\nu\nu'\nu''}$ is the Levi-Civita symbol for SU(2) and $\sigma^{(\nu)}$ are the Pauli matrices.

To represent these operators in a matrix form, it is useful to express them in the chromoelectric basis of states $|jm_L m_R\rangle$, where $j \in \mathbb{N}/2$ labels the spin-irreducible representations (irreps), $m_R \in \{-j, .., j\}$ labels a spin shell j, and $m_L \in \{-j, .., j\}$ labels a state within the spin shell adjoint to j. The gauge-field algebra operators in this basis [81],

$$
\begin{aligned}
&\langle j'm'_L m'_R|\hat{E}^2|jm_L m_R\rangle = j(j+1)\delta_{j,j'}\delta_{m_L,m'_L}\delta_{m_R,m'_R}, \\
&\langle j'm'_L m'_R|\hat{U}^{ab}|jm_L m_R\rangle = \left(C^{j,m_L}_{j',m'_L;\frac{1}{2},a}\right)^* C^{j',m'_R}_{j,m_R;\frac{1}{2},b},
\end{aligned}
\tag{3}
$$

where $C^{J,M}_{j_1,m_1;j_2,m_2} = \langle j_1, m_1; j_2, m_2|J, M\rangle$, are the Clebsch-Gordan coefficients, i.e., the fusion rules, for SU(2).

The model given in Eq. (1) is designed to be symmetry invariant under the gauge transformations generated by $\hat{\mathbf{G}}_n = \left(\hat{\mathbf{R}}_{n-1,n} + \hat{\mathbf{S}}_n + \hat{\mathbf{L}}_{n,n+1}\right)$, where $\hat{S}^{(\nu)}_n = \frac{1}{2}\sum_{a,b}\sigma^{(\nu)}_{ab}\hat{\psi}^\dagger_{na}\hat{\psi}_{nb}$ generates the color rotations for the quarks. Under this observation, the non-Abelian Gauss's law, which defines the sector of physical states $|\Psi_{\text{phys}}\rangle$, reads

$$
\left|\hat{\mathbf{G}}_n\right|^2 |\Psi_{\text{phys}}\rangle = 0 \; \forall n \qquad \text{(Gauss's law)}, \tag{4}
$$

corresponding to the absence of a color background.

A. Hardcore-gluon approximation

To digitally quantum simulate the Hamiltonian in Eq. (1), it is necessary to truncate the infinite local gauge Hilbert space to a finite dimension. This can be done at low energies by employing the quantum link model (QLM) [82] formalism, where only a finite set of shells j are considered. Basically, a cutoff is chosen for the $\hat{E}^2$ energy term and the spin shells j above the cutoff are discarded. Our proposal for digital quantum simulation considers a QLM cutoff that includes the $j = 0$ and $j = \frac{1}{2}$ shells, i.e., the smallest cutoff that allows quarks to form bound states of baryons and mesons. In practice, in our descriptions we keep all the states that are reachable from the bare vacuum with a single application of $\hat{U}^{ab}$: in analogy to cold-atom physics, we refer to this cutoff strategy as "hardcore gluons" and it is a reasonable approximation for strong-coupling regimes [50,51, 83]. Ultimately, this picture describes a five-dimensional gauge-field Hilbert space at each bond, spanned by the link basis set $\{|00\rangle, |rr\rangle, |gg\rangle, |gr\rangle, |rg\rangle\}$. Within this representation, it is possible to decompose each gauge-field bond into a pair of rishons. Then, the parallel transporter can be efficiently decomposed as $\hat{U}^{ab}_{n,n+1} = (1/\sqrt{2})(\hat{\zeta}^a_{n,n+1})_L(\hat{\zeta}^{b\dagger}_{n,n+1})_R$, where each of the exotic fermions $\hat{\zeta}^a$ lives on the left (L) and right (R) rishon of the same link, as sketched in the second row of Fig. 1(a). Each rishon mode is ultimately three-dimensional, spanned by the state $|0\rangle = |j = 0, m = 0\rangle$ with even fermion parity $\langle\hat{P}\rangle = +1$, and the states $|r\rangle = |j = \frac{1}{2}, m = +\frac{1}{2}\rangle$, $|g\rangle = |j = \frac{1}{2}, m = -\frac{1}{2}\rangle$ with odd fermion parity $\langle\hat{P}\rangle = -1$. In this representation, the fermion parity on a link becomes an Abelian (gauge $\mathbb{Z}_2$) symmetry of the dynamics, which defines the five-dimensional space. By contrast, the matter sites are regular Dirac fermions, thus spanned by the site basis: $|0\rangle$, the fermion vacuum (even fermion parity); $|r\rangle = \hat{\psi}^\dagger_r|0\rangle$ and $|g\rangle = \hat{\psi}^\dagger_g|0\rangle$, singly occupied states (odd parity); and, finally, $|d\rangle = \hat{\psi}^\dagger_r\hat{\psi}^\dagger_g|0\rangle$, the doubly occupied state (even). We can now fuse together the (R)$_{n-1,n}$ rishon, the matter at site n, and the (L)$_{n,n+1}$ rishon into a unique dressed site. We now enforce the non-Abelian Gauss's law of Eq. (4), resulting in an effective six-dimensional gauge-invariant basis for the dressed site, defined as the tensor product of the matter field on a lattice site and of the rishon states on its left and right. This basis, pictorially sketched in Fig. 1(b), contains only states with even total fermion parity and explicitly reads

$$
\begin{aligned}
&|1\rangle = |0,0,0\rangle, &&|2\rangle = \frac{|r,0,g\rangle - |g,0,r\rangle}{\sqrt{2}}, \\
&|3\rangle = \frac{|g,r,0\rangle - |r,g,0\rangle}{\sqrt{2}}, &&|4\rangle = \frac{|0,r,g\rangle - |0,g,r\rangle}{\sqrt{2}}, \\
&|5\rangle = |0,d,0\rangle, &&|6\rangle = \frac{|r,d,g\rangle - |g,d,r\rangle}{\sqrt{2}}.
\end{aligned}
\tag{5}
$$

TABLE I.   Four of the six matrices that define the effective model on qudits. These four are related to the covariant Dirac transport and they are factors of a nearest-neighbor interaction $\hat{A}_n^{(1)}\hat{B}_{n+1}^{(1)} + \hat{A}_n^{(2)}\hat{B}_{n+1}^{(2)}$.

$\hat{A}^{(1)}$	$\hat{A}^{(2)}$	$\hat{B}^{(1)}$	$\hat{B}^{(2)}$
$\begin{pmatrix} 0 & & \sqrt{2} & & & \\ & 0 & 1 & & & \\ 1 & 0 & & \sqrt{2} & & 1 \\ \sqrt{2} & & 0 & \sqrt{2} & & \\ & \sqrt{2} & 0 & & & \\ & & 1 & & & 0 \end{pmatrix}$	$\begin{pmatrix} 0 & & \sqrt{2}i & & & \\ & 0 & i & & & \\ -i & 0 & & \sqrt{2}i & & i \\ -\sqrt{2}i & & 0 & \sqrt{2}i & & \\ & -\sqrt{2}i & 0 & & & \\ & & -i & & & 0 \end{pmatrix}$	$\begin{pmatrix} 0 & & -\sqrt{2}i & & & \\ & 0 & & -i & & \\ \sqrt{2}i & 0 & & -\sqrt{2}i & & \\ i & & 0 & & -i & \\ & \sqrt{2}i & & 0 & & \\ & & i & & & 0 \end{pmatrix}$	$\begin{pmatrix} 0 & & \sqrt{2} & & & \\ & 0 & & 1 & & \\ \sqrt{2} & 0 & & \sqrt{2} & & \\ 1 & & 0 & & 1 & \\ & \sqrt{2} & & 0 & & \\ & & 1 & & & 0 \end{pmatrix}$

As such, the model preserves fermion parity at each dressed site [84]. In this dressed-site basis, it is relatively straightforward (see Appendix A) to rewrite the hardcore-gluon SU(2) Yang-Mills model from Eq. (1) into an effective Hamiltonian,

$$
\hat{H} = \sum_n \left[\hat{A}_n^{(1)}\hat{B}_{n+1}^{(1)} + \hat{A}_n^{(2)}\hat{B}_{n+1}^{(2)} \right] + m \sum_n (-1)^n \hat{M}_n \\
+ g^2 \sum_n \hat{C}_n, \tag{6}
$$

where we set the energy scale based on the hopping term, by rescaling $\hat{H}_0 \to \hat{H} = ((4\sqrt{2}a_0)/c\hbar)\hat{H}_0$, to work in natural units, with a dimensionless Hamiltonian $\hat{H}$ and dimensionless couplings $m = ((4\sqrt{2}m_0 a_0 c)/\hbar)$ and $g^2 = ((3\sqrt{2})/4)g_0^2$. The 6×6 matrix operators appearing in this expression are reported in Tables I and II.

While the non-Abelian Gauss's law has been already enforced in the definition of a dressed basis, we still have to take into account the link law, which has arisen from splitting a gauge field into two rishons. In the effective model, the link law translates into an Abelian selection rule,

$$
\left(\hat{D}_n^{(L)}\hat{D}_{n+1}^{(R)} - 1 \right) |\Psi_{\text{phys}}\rangle = 0 \ \forall n \qquad \text{(link law)}. \tag{7}
$$

This symmetry at each link is protected by the Hamiltonian; thus, in principle, it would be sufficient to satisfy the constraint on the initial state of the dynamics. However, this symmetry may be disrupted by noise and imperfections in a digital quantum simulator [30,32]. In Sec. V B,

we discuss how to mitigate this error via a postselection procedure.

Another important symmetry to discuss is the conservation of the total baryon number $\hat{N}_b = \frac{1}{2}\sum_n(\hat{M}_n - 1)$. This quantity can be controlled by appropriately constructing the starting state of the dynamics and allows the quantum simulator to explore areas of the phase diagram, with high baryon density, inaccessible to Monte Carlo simulations due to the sign problem.

III. ENCODING INTO TRAPPED-ION QUDITS

The structure of the truncated gauge-preserving Hamiltonian given in Eq. (6), defined on a dressed local basis of dimension six, suggests a natural implementation on a qudit-based quantum processor. In the following, we focus on an implementation using trapped $^{40}\text{Ca}^+$ ions, as presented in Ref. [69], but the proposed scheme is versatile and also applicable to other qudit quantum processors. In the trapped-ion experiment of Ref. [69], each qudit is encoded within the electronic ground state $S_{1/2}$ and the metastable excited state $D_{5/2}$, as illustrated in Fig. 2. An external magnetic field splits the $S_{1/2}$ state into two Zeeman sublevels, $m_B = \pm 1/2$, and the excited state into six Zeeman sublevels ($m_B = \pm 5/2, \pm 3/2, \pm 1/2$). This configuration yields a total of eight accessible qudit levels connected, considering the selection rules, by ten allowed electric-quadrupole transitions ($\Delta m_B = 0, \pm 1, \pm 2$). A convenient encoding of the model given in Eq. (6) onto the levels of the ion involves placing the states $|3\rangle$ and $|4\rangle$ within the $S_{1/2}$ ground state,

TABLE II.   The last two matrices that define the effective model, related to mass term (before staggerization) and the chromoelectric energy density, respectively. The table also shows the matrices of the link fermion-parity selection rule.

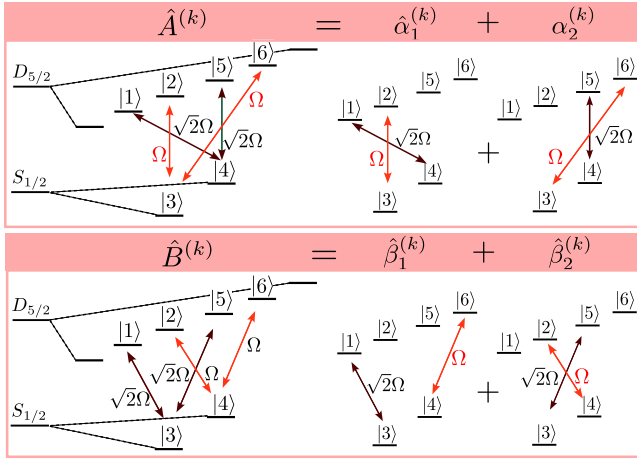| $\hat{M}$	$\hat{C}$	$\hat{D}^{(L)}$	$\hat{D}^{(R)}$
$\begin{pmatrix} 0 & & & & & \\ & 0 & & & & \\ & & 1 & & & \\ & & & 1 & & \\ & & & & 2 & \\ & & & & & 2 \end{pmatrix}$	$\begin{pmatrix} 0 & & & & & \\ & 2 & & & & \\ & & 1 & & & \\ & & & 1 & & \\ & & & & 0 & \\ & & & & & 2 \end{pmatrix}$	$\begin{pmatrix} +1 & & & & & \\ & -1 & & & & \\ & & +1 & & & \\ & & & -1 & & \\ & & & & +1 & \\ & & & & & -1 \end{pmatrix}$	$\begin{pmatrix} +1 & & & & & \\ & -1 & & & & \\ & & -1 & & & \\ & & & +1 & & \\ & & & & +1 & \\ & & & & & -1 \end{pmatrix}$

FIG. 2. Model encoding into ions qudit. The six states needed for the model given in Eq. (6) are encoded within the eight Zeeman sublevels of the $S_{1/2}$ and $D_{5/2}$ states of ^{40}Ca$^+$ ions. By encoding the states $|3\rangle$ and $|4\rangle$ into the $S_{1/2}$ manifold, all matrix elements can be implemented via direct transitions. The boxes on the left show the driving scheme to implement the $\hat{A}^{(k)}$ and $\hat{B}^{(k)}$ matrices, $k = 1, 2$, while the boxes on the right show the implementation of the $\hat{\alpha}^{(k)}$ and $\hat{\beta}^{(k)}$ matrices. The relative Rabi frequencies needed for each transition are indicated next to the corresponding arrows with two different colors, red for Ω and dark red for $\sqrt{2}\Omega$.

while the remaining states reside in the $m_B = \pm 3/2$ and $m_B = \pm 1/2$ levels of the $D_{5/2}$ metastable state, as illustrated in Fig. 2. This choice is motivated by the observation that all the transitions in the model are interconnected via the two states: $|3\rangle$ and $|4\rangle$. Note that compared to other encoding strategies [71–73], where each gauge link and each fermion site are separately associated with a qudit, our approach only requires N qudits to describe both gauge and matter fields in a lattice consisting of N sites. Such a reduction in the number of employed atoms is an important advantage for ion-based simulators, where scalability in the number of atoms is a standing challenge.

Let us now discuss the implementation of the different terms composing the qudit Hamiltonian given in Eq. (6). Generic single-qudit operations among these states can be decomposed into at most $d(d-1)/2$ two-level subspace rotations, where d is the qudit dimension. These rotations have the form $\hat{R}(\theta, \phi) = e^{-i(\theta/2)\hat{\sigma}_\phi^{s,s'}}$, where the operators $\hat{\sigma}_\phi^{s,s'} = |s\rangle\langle s'|$ connect the qudit states s and s', θ denotes the rotation angle, and ϕ sets the rotation axis. Importantly, in the model defined in Eq. (6) the mass and gauge Hamiltonians are diagonal, requiring only five elementary rotations, which can be easily implemented with high fidelity.

The hopping part of the Hamiltonian given in Eq. (6) is more demanding. It necessitates two-qudit operations, which can be broken down into a sequence of entangling gates operating on pairs of qudit levels (we omit the site

subscript n for notational simplicity):

$$
\begin{aligned}
\hat{A}^{(1)} &= \hat{\sigma}_x^{2,3} + \sqrt{2}\hat{\sigma}_x^{1,4} + \sqrt{2}\hat{\sigma}_x^{4,5} + \hat{\sigma}_x^{3,6}, \\
\hat{A}^{(2)} &= -\left(\hat{\sigma}_y^{2,3} + \sqrt{2}\hat{\sigma}_y^{1,4} + \sqrt{2}\hat{\sigma}_y^{4,5} + \hat{\sigma}_y^{3,6}\right), \\
\hat{B}^{(1)} &= \hat{\sigma}_y^{2,4} + \sqrt{2}\hat{\sigma}_y^{1,3} + \sqrt{2}\hat{\sigma}_y^{3,5} + \hat{\sigma}_y^{4,6}, \\
\hat{B}^{(2)} &= \hat{\sigma}_x^{2,4} + \sqrt{2}\hat{\sigma}_x^{1,3} + \sqrt{2}\hat{\sigma}_x^{3,5} + \hat{\sigma}_x^{4,6}.
\end{aligned}
\tag{8}
$$

Note that with the chosen encoding of the model, this decomposition involves only direct transitions between the $S_{1/2}$ and $D_{5/2}$ states. From this decomposition, it becomes evident that a single next-neighbor $(n, n+1)$ block of the hopping Hamiltonian requires a total of 32 entangling gates of the form $\hat{R}_{XY}(\varphi) = e^{-i\varphi\hat{\sigma}_x^{s_1,s_2}\otimes\hat{\sigma}_y^{s_3,s_4}}$. These rotations can be implemented using MS gates [85]. Although this decomposition requires resources available on the current trapped-ion-qudit quantum processor [69], the considerable gate count imposes limitations on the performance of a quantum simulation of the model. In the following, we will explore how this scheme can be enhanced by using native qudit gates based on the simultaneous driving of multiple transitions.

A. Native two-qudit gates

The two hopping blocks, denoted as $\hat{A}_n^{(k)}\hat{B}_{n+1}^{(k)}$ with $k = 1, 2$, can be directly implemented through a generalized MS scheme [79] that involves the simultaneous driving of all four direct transitions in each ion, as depicted in Fig. 2. Similar to standard MS gates, we assume that each transition of interest, $\omega_{s,s'}$, is driven by a pair of lasers with frequencies ω_L^1 and ω_L^2, featuring opposite detunings, i.e., $\omega_L^1 = \omega_{s,s'} + \delta$ and $\omega_L^2 = \omega_{s,s'} - \delta$. To achieve the correct matrix elements reported in Table I, two out of the four transitions are driven with a Rabi frequency of Ω, while the other two are driven with $\sqrt{2}\Omega$ (see Fig. 2). Additionally, the phases ϕ_n associated with the driving of each ion are chosen to align with the correct phase pattern. We assume that we are working in the Lamb-Dicke regime, $\eta \ll 1$, with η being the Lamb-Dicke parameter, and that we separate the blue and red sidebands, coming from each laser pair, via a rotating-wave approximation that is valid in the regime in which the lasers are tuned close to the motional sideband with frequency ν, i.e., $|\delta - \nu| \ll \delta$. A hopping block for two target ions n and $n+1$ can then be implemented via the generalized MS Hamiltonian

$$
\hat{\bar{H}}_{\hat{A}_n\hat{B}_{n+1}}^{(k)} = \hbar\frac{\eta\Omega}{2}\left[\hat{A}_n^{(k)} + \hat{B}_{n+1}^{(k)}\right][\hat{a}^\dagger e^{i(\nu-\delta)t} + \hat{a}e^{-i(\nu-\delta)t}],
\tag{9}
$$

where $\hat{a}$ ($\hat{a}^\dagger$) is the phonon annihilation (creation) operator. In the regime of weak driving, $\eta\Omega \ll |\nu - \delta|$, the phononic

bath dispersively mediates interactions among the two ions according to the effective Hamiltonian

$$\hat{\tilde{H}}^{(k)}_{\hat{A}_n \hat{B}_{n+1}} \simeq \hbar \frac{(\eta \Omega)^2}{4(\nu - \delta)} \left[\hat{A}^{(k)}_n + \hat{B}^{(k)}_{n+1} \right]^2, \qquad (10)$$

where, in order to minimize the population of the motional mode, we have assumed that we can let the system evolve for a time $d\bar{t} = 2\pi \ell / |\nu - \delta|$, with ℓ being a positive integer [79,85]. To perform the dynamics in natural units, as in Eq. (6), we rescale this time by the rate associated with the MS gate, i.e., $d\bar{t} \to dt = \pi (\eta \Omega / |\nu - \delta|)^2$. The Hamiltonian given in Eq. (10), once rescaled, exactly reproduces the desired hopping block up to unwanted single-qudit rotations coming from the terms $(\hat{A}^{(k)}_n)^2$ and $(\hat{B}^{(k)}_{n+1})^2$. Upon aggregating contributions from all transitions, these rotations simplify to straightforward diagonal matrices. These terms can then be combined with the mass and gauge Hamiltonians of Eq. (6), resulting in the following single-qudit Hamiltonian:

$$\hat{H}_n = m(-1)^n \hat{M}_n + g^2 \hat{C}_n - \hat{H}^{A^2}_n - \hat{H}^{B^2}_n, \qquad (11)$$

where the diagonal terms in natural units read

$$\begin{aligned}
\hat{H}^{A^2}_n &= \text{diag}(2, 1, 2, 4, 2, 1), \\
\hat{H}^{B^2}_n &= \text{diag}(2, 1, 4, 2, 2, 1).
\end{aligned} \qquad (12)$$

Note that for $n = 1$, besides the gauge and mass terms, only $\hat{H}^{A^2}_n$ contributes to the Hamiltonian in Eq. (11), while for $n = N$ only the $\hat{H}^{B^2}_n$ term contributes. The Hamiltonian terms given in Eqs. (10) and (11) constitute the fundamental building blocks of the digital quantum simulation to be discussed in Sec. V. Importantly, with this procedure involving generalized MS gates based on the simultaneous driving of four transitions, only two entangling operations (one per each hopping block) are necessary to implement the hopping between two neighboring sites.

B. Intermediate scheme

The native qudit-gate scheme outlined in Sec. III A offers the advantage of achieving an exceptionally short circuit depth. Nevertheless, the implementation of this method presents technical challenges, primarily stemming from the requirement for fine-tuned calibration of all driven transitions (see Sec. VI). Fortunately, this demand can be avoided by an intermediate scheme relying on the simultaneous driving of only two distinct disjoint transitions. The core idea involves decomposing the interaction matrices as $\hat{A}^{(k)} = \hat{\alpha}^{(k)}_1 + \hat{\alpha}^{(k)}_2$ and $\hat{B}^{(k)} = \hat{\beta}^{(k)}_1 + \hat{\beta}^{(k)}_2$,

where $k = 1, 2$ and

$$\begin{aligned}
\hat{\alpha}^{(1)}_1 &= \hat{\sigma}^{2,3}_x + \sqrt{2}\hat{\sigma}^{1,4}_x, & \hat{\alpha}^{(2)}_1 &= -\left(\hat{\sigma}^{2,3}_y + \sqrt{2}\hat{\sigma}^{1,4}_y \right), \\
\hat{\alpha}^{(1)}_2 &= \hat{\sigma}^{3,6}_x + \sqrt{2}\hat{\sigma}^{4,5}_x, & \hat{\alpha}^{(2)}_2 &= -\left(\hat{\sigma}^{3,6}_y + \sqrt{2}\hat{\sigma}^{4,5}_y \right), \\
\hat{\beta}^{(1)}_1 &= \hat{\sigma}^{4,6}_y + \sqrt{2}\hat{\sigma}^{1,3}_y, & \hat{\beta}^{(2)}_1 &= \hat{\sigma}^{4,6}_x + \sqrt{2}\hat{\sigma}^{1,3}_x, \\
\hat{\beta}^{(1)}_2 &= \hat{\sigma}^{2,4}_y + \sqrt{2}\hat{\sigma}^{3,5}_y, & \hat{\beta}^{(2)}_2 &= \hat{\sigma}^{2,4}_x + \sqrt{2}\hat{\sigma}^{3,5}_x,
\end{aligned} \qquad (13)$$

is one of the possible decompositions involving only disjoint transitions. The following discussion still holds for other possible decomposition choices. With this scheme, in contrast to the earlier approach involving only two entangling gates, a total of eight operations are required to reproduce the hopping between two neighboring sites. The different contributions can be once again implemented by simultaneously driving the two target transitions with a pair of bichromatic pulses characterized by Rabi frequencies $(\Omega, \sqrt{2}\Omega)$, as illustrated in Fig. 2. Assuming the validity of the same assumptions as employed in Sec. III A, we derive the effective Hamiltonian

$$\hat{\tilde{H}}^{(k)}_{\hat{\alpha}_{q,n} \hat{\beta}_{q',n+1}} \simeq \hbar \frac{(\eta \Omega)^2}{4(\nu - \delta)} \left[\hat{\alpha}^{(k)}_{q,n} + \hat{\beta}^{(k)}_{q',n+1} \right]^2, \qquad (14)$$

where $q, q' = 1, 2$ and we again set the time step to $d\bar{t} = 2\pi \ell / |\nu - \delta|$. As before, the phonon-mediated interaction induces unwanted single-qudit transitions that reduce, after rescaling in the natural units, to twice the same diagonal matrices of in Eq. (12), $\hat{H}_n = m(-1)^n \hat{M}_n + g^2 \hat{C}_n - 2\hat{H}^{A^2}_n - 2\hat{H}^{B^2}_n$.

IV. MODEL PHENOMENOLOGY

In this section, we consider a few paradigmatic examples of nontrivial dynamics occurring in the model by evolving the initial state $|\Psi(t = 0)\rangle$ under the time-dependent Schrödinger equation ruled by the Hamiltonian given in Eq. (6). In particular, we identify phenomena and observables where the non-Abelian nature of the theory manifests itself with distinctive features and that could be implemented in current state-of-the-art experiments.

A. Vacuum fluctuations

We first consider the phenomena of particle-density fluctuations starting from an initial false vacuum [16,19,37]. Let us assume the system to be initially in the Dirac sea, i.e., the bare vacuum represented by the ground state of the free part of the Hamiltonian given in Eq. (6) for large positive mass and coupling, which consists in alternating empty and doubly occupied quark and antiquark sites, $|\Psi(t = 0)\rangle = |5\rangle|1\rangle \ldots |5\rangle|1\rangle$. When the hopping turns on, this state no longer represents the real ground state and

it undergoes a nontrivial dynamical evolution: depending on the Hamiltonian parameters, spontaneous production of quark-antiquark pairs out of the vacuum takes place. This effect can be quantified by the lattice particle-density counting for the total number of created quark and antiquark excitations,

$$\rho(t) = \rho_s(t) + \rho_d(t), \tag{15}$$

where the $\rho_e(t) = 1/(2N) \sum_n p_e(n, t)$ represent, respectively, the single- ($e = s$) and double- ($e = d$) particle-occupancy densities computed from the probability distributions:

$$p_s(n, t) = |\langle \Psi(t)|3\rangle_n|^2 + |\langle \Psi(t)|4\rangle_n|^2, \tag{16}$$

and

$$p_d(n, t) = 2 \begin{cases} |\langle \Psi(t)|5\rangle_n|^2 + |\langle \Psi(t)|6\rangle_n|^2, & \text{if } n \in \text{even}, \\ |\langle \Psi(t)|1\rangle_n|^2 + |\langle \Psi(t)|2\rangle_n|^2, & \text{if } n \in \text{odd}. \end{cases} \tag{17}$$

In Fig. 3(a)(i), we simulate the evolution of the particle density for different mass-coupling ratios starting from the Dirac sea. For small masses, $m \ll 1$, particle production

is energetically favorable and after a transient the system reaches a steady state with approximately one particle per lattice site. For large masses, $m \gg 1$, instead, the particle production is more expensive and recombination effects let the system oscillate between the Dirac and the true vacuum. To probe the non-Abelian nature of the model, we compute separately the contributions to the particle density coming from the single- and double-particle-occupancy densities. In turn, these quantities encode the population of bare excitations such as color-singlet pairs formed by a quark and an antiquark occupying two neighboring sites with an excited shared gauge link (bare meson) and quark-quark (bare-baryon) or antiquark-antiquark (bare-antibaryon) pairs occupying the same site. Note that the baryon population is absent in Abelian models where just one particle can be hosted in each lattice site. To quantify the different weights of the two contributions to the total particle density, we plot in Fig. 3(a)(ii) the difference between the double- and single-particle-occupation densities as a function of time for the same mass-coupling ratios as in Fig. 3(a)(i). The figure shows how single-particle occupation is dominant in the weak-coupling regime, $g^2 \ll 1, m$, while in the strong-coupling regime, $g^2 \gg 1, m$, the production of bare baryons is more energetically favorable. Such baryon production has no analogues in Abelian
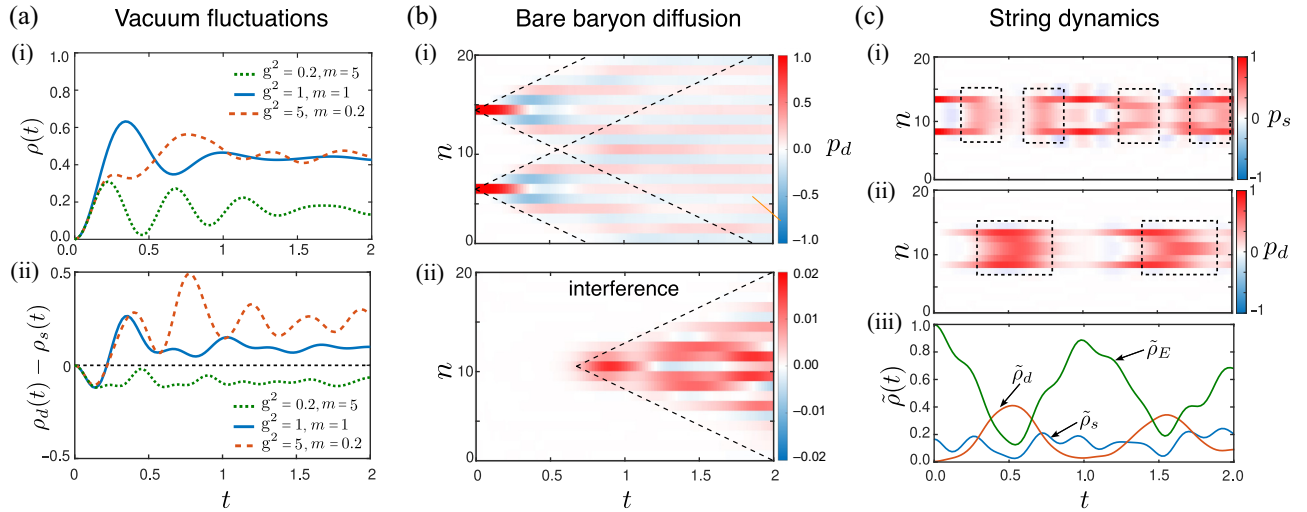

FIG. 3. Model phenomenology. (a) Vacuum fluctuations: (i) the particle density and (ii) the difference between the double- and single-particle-occupancy densities as a function of time, for different mass-coupling values as indicated in the figure. (b) Bare-baryon diffusion. (i) The double-occupancy probability distribution as a function of time, capturing the evolution of two bare baryons initially excited at positions $n = 6$ and $n = 14$ with $g^2 = m = 0.5$. To better resolve the dynamics, we have subtracted the probability distribution associated with the evolution of the vacuum state. (ii) The interference pattern of the process described in (i), obtained by subtracting the individual diffusion of each baryon. (c) String dynamics. The (i) single- and (ii) double-occupancy probability distributions as a function of time, for a quark-antiquark string initially excited within the sites $n = 8 - 13$ with $g^2 = m = 5$. Here, we have again subtracted the vacuum-state evolution. (iii) The electric field and single- and double-occupancy string densities as a function of time, for the same scenario as in panels (i) and (ii). All the simulations have been carried out for a lattice of $N = 20$ sites, solving the dynamics of the model given in Eq. (6), with matrix product states setting the truncation tolerance to tol $= 10^{-7}$ and the maximum bond dimension to $D_{\text{max}} = 200$.

theories and is a clear signature of the underlying SU(2) nature of the model.

B. Bare-baryon diffusion

The second dynamical phenomenon under consideration involves the diffusion of two pairs of quarks (bare baryons) initially localized on two even sites of the lattice, with the rest of the system being in the Dirac vacuum. In the strong-coupling limit, where $g \gg m, 1$, these pairs play the role of composite particles in the lattice, hopping from one matter site to another, weakly exciting all other allowable configurations. This regime, characterized by a fourth-order process with a rate of $J_{\mathrm{eff}} = 16/g^4 m$, occurs on a time scale significantly longer than the natural unit (see Appendix B). Consequently, it is not practically feasible for digital quantum simulation, due to the requirement for numerous time steps (see Sec. V).

To investigate baryon diffusion on a shorter time scale, we examine the nonperturbative regime in which $g \sim m \lesssim 1$. Specifically, we focus on the scenario in which two bare baryons are initially excited out of the Dirac vacuum, $\hat{S}_{n_1}^{51} \hat{S}_{n_2}^{51} |\mathrm{GS}\rangle$, where $\hat{S}_n^{ss'} = |s\rangle\langle s'|_n$, with n_1 and n_2 being even numbers. In Fig. 3(b)(i), the evolution of the double-occupancy probability distribution, p_d, is plotted, with the vacuum fluctuation subtracted to reveal the diffusion process. The two bare baryons disperse within a wave-front cone with an aperture of approximately $\pm 8t$, governed by the quark hopping rate. The interference of the two bare baryons is depicted in Fig. 3(b)(ii) and is obtained by subtracting the individual bare-baryon propagations.

C. String dynamics

Finally, we consider the dynamics of an initially excited string. In this context, string breaking is a typical phenomenon occurring in confined LGTs, where an initial string excitation undergoes evolution by breaking into pairs of particles and antiparticles. This phenomenon has been extensively studied numerically in (1+1)D U(1) models [35,37–39] and in a (1+1)D SU(2) theory using a different rishon representation than the one employed here [47]. To initialize the state configuration, we apply the following string operator of length l to the Dirac-sea vacuum: $\hat{S} = \hat{\psi}_{n_s}^\dagger \hat{U}_{n_s,n_s+1}, \ldots \hat{U}_{n_s+l-1,n_s+l} \hat{\psi}_{n_s+l}$, where we assume n_s to be even, corresponding to the creation of a quark, and $n_s + l$ to be odd, corresponding to the creation of an antiquark on that site. Expressed in the local dressed basis of Eq. (5), this string reads

$$\hat{S} = \hat{S}_{n_s}^{41} \hat{S}_{n_s+1}^{65} \hat{S}_{n_s+2}^{21} \cdots \hat{S}_{n_s+l-2}^{65} \hat{S}_{n_s+l-1}^{21} \hat{S}_{n_s+l}^{35}. \tag{18}$$

Here, we again focus on distinctive non-Abelian features by distinguishing between bare-meson and -baryon resonant production from the string. To observe resonant production of bare baryons and mesons, we consider the

case in which the initial string of energy $E_{\mathrm{str}} = 2m + 2lg^2$ resonates with the energy of $l + 1$ baryons, each having energy $E_{\mathrm{bar}} = 2m$, and $(l + 1)/2$ mesons, each having energy $E_{\mathrm{mes}} = 2m + 2g^2$. This resonance condition is fulfilled for both processes when $g^2 = m$. We then let the system evolve in time with fixed mass and coupling set to large values to ensure that most of the energy remains confined within the string, preventing quick dispersion toward the system edges. In Fig. 3(c), we indeed observe resonant excitations in time of the single- and double-occupancy probability distributions within the string, signaling the creation of the string of bare baryons and mesons. These resonant oscillations are better resolved in Fig. 3(c)(iii), where we plot the single- $(e = s)$ and double- $(e = d)$ occupancy densities averaged within the string, $\tilde{\rho}_e(t) = 1/(2(l+1)) \sum_{n=n_s}^{n_s+l} p_e(n, t)$, along with the electric field string density, defined as

$$\tilde{\rho}_E = \frac{1}{2l} \sum_{n=n_s}^{n_s+l-1} |\langle \Psi(t)|2\rangle_n|^2 + |\langle \Psi(t)|4\rangle_n|^2 + |\langle \Psi(t)|6\rangle_n|^2$$
$$+ |\langle \Psi(t)|2\rangle_{n+1}|^2 + |\langle \Psi(t)|3\rangle_{n+1}|^2 + |\langle \Psi(t)|6\rangle_{n+1}|^2, \tag{19}$$

which accounts for the number of rishons on each link.

V. DIGITAL QUANTUM SIMULATION

In this section, we explore how the dynamics previously described can be simulated digitally using a trapped-ion-qudit quantum processor. To digitally simulate the dynamics, we use the first-order Suzuki-Trotter decomposition

$$\hat{\mathcal{U}}(t_{\mathrm{f}}) = e^{-i\hat{H}t_{\mathrm{f}}} \simeq \left(\prod_j e^{-i\hat{h}_j \, dt} \right)^{n_{\mathrm{ST}}}, \tag{20}$$

where $dt = t_{\mathrm{f}}/n_{\mathrm{ST}}$ denotes the time step ruling the precision of the Suzuki-Trotter evolution, n_{ST} is the number of Suzuki-Trotter steps, and t_{f} is the final time of the evolution. The terms h_j represent the Hamiltonian building blocks composing the Hamiltonian given in Eq. (6), which we have presented in Sec. III. The evolution of the model is then obtained by executing, for each time step, the unit-cell circuit (in parallel across the lattice), depicted in Fig. 4 for both schemes presented in Sec. III. The unit-cell circuit involves three lattice sites and is composed of the generalized MS gates, implementing the hopping part of the model, followed by a single-qudit rotation on each ion encompassing the gauge and mass terms of the Hamiltonian given in Eq. (11) and the correcting rotations. Considering that single-qudit rotations can be performed with high fidelity, we define the circuit depth of the model, $\mathcal{D}$, as the number of generalized MS gates per unit-cell circuit. Then, the total number of two-qudit gates, N_{gates}, required

to perform the entire simulation on a chain of N sites scales linearly with the system size and the Trotter steps:

$$N_{\text{gates}} = \frac{(N-1)}{2} n_{\text{ST}} \mathcal{D}, \tag{21}$$

where $\mathcal{D} = 4$ and $\mathcal{D} = 16$, respectively, for the first and second schemes presented in Sec. III. Note that the total gate count of our proposal for both schemes is drastically reduced with respect to a computation based on a decomposition into two-level entangling gates (see Sec. III), which has $\mathcal{D} = 64$.

For a realistic numerical simulation of the model, we consider small lattice sizes, specifically $N = 3$ and $N = 4$. These sizes are chosen as they retain the essential characteristics of the SU(2) dynamics under consideration while being accessible with a short circuit implementation. The generalized MS gates are simulated explicitly including the vibrational degree of freedom using the Hamiltonian in Eq. (9) and its analogue for the intermediate scheme.

A. Reproducing the system dynamics

To assess the performance of the proposed quantum digital simulation, we compare the results of the exact expected dynamics with those derived from the digital scheme. We apply this comparison to the same illustrative examples of dynamics discussed in Sec. IV. As a first example, we consider in Fig. 4 the particle-density evolution of the Dirac vacuum on $N = 3$ lattice sites for the two schemes outlined in Sec. III. To perform a comparison with the exact evolution, we also compute the state fidelity, $\mathcal{F}(t) = \langle \Psi(t) | \hat{\varrho}_q(t) | \Psi(t) \rangle$, where $\hat{\varrho}_q(t)$ represents the reduced density operator of the qudit system after tracing over the phononic degrees of freedom and

$|\Psi(t)\rangle$ is the state evolved under the Schrödinger equation. The performance of the two schemes is comparable, with the precision of the simulation ruled by the Suzuki-Trotter step dt. Importantly, even for large time steps, $dt = 0.04\pi$, the initial density peak, arising from particle production and characterizing the response time of the system, can be accurately approximated with just $n_{\text{ST}} = 3$ Suzuki-Trotter steps. Higher simulation precision can be reached by performing a second-order Suzuki-Trotter decomposition, as presented in Appendix C and discussed in Sec. VI.

Despite the limited lattice size, the digital simulation effectively captures distinct production rates for paired (doubly occupied sites) and unpaired (singly occupied sites) particles. This is exemplified in Fig. 5(a), where we observe a phenomenology that is similar to the one depicted in Fig. 3(a) for the disparity between double- and single-particle occupation densities. In addition to particle production from the vacuum, the digital simulation, when confined to a few lattice sites, successfully replicates the other two phenomena discussed in Sec. IV: bare-baryon diffusion and string dynamics. The former is illustrated in Fig. 5(b), where we consider the hopping of a bare antibaryon excited on the first site toward the third site. This process is quantified by observing the double-particle-occupancy probability on the first lattice site, involving an intermediate single-particle population on the second site. To enhance the resolution of this effect, we have subtracted the Dirac vacuum evolution from the simulation, consistent with the approach taken in Sec. IV. The final phenomenon under consideration is string breaking. For this scenario, we extend our analysis to a slightly larger system size, specifically $N = 4$. Proceeding as in Fig. 3(c)(iii), we calculate the electric field, as well as the densities of the single- and double-occupancy strings,
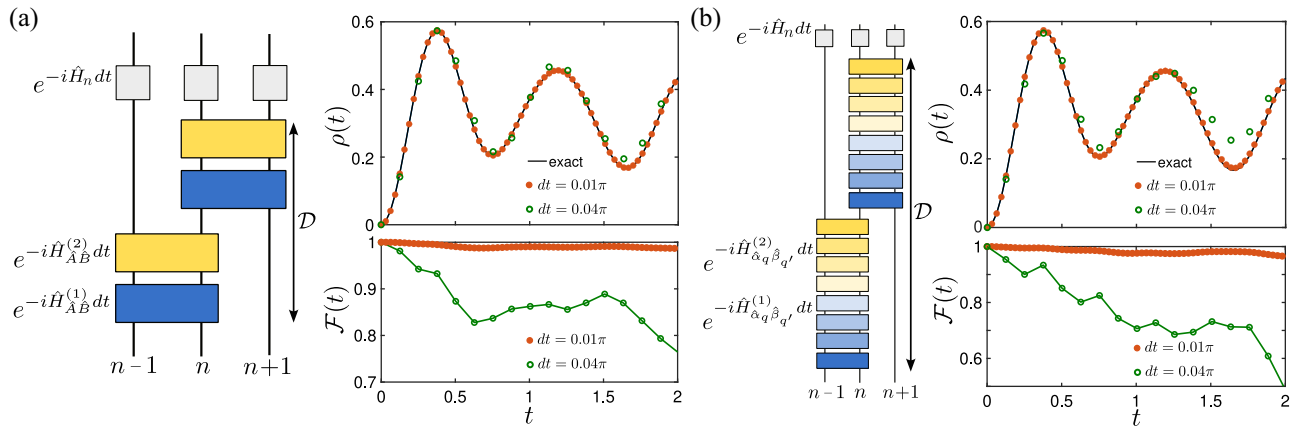

FIG. 4. Digital quantum simulation. (a),(b) Left panels: the circuit decomposition for the two strategies outlined in the text, (a) the full and (b) the intermediate scheme. In both, $\mathcal{D}$ indicates the circuit depth. Right panels: the dynamics of the particle density evolving from the Dirac vacuum for $N = 3$ lattice sites obtained through the model given in Eq. (6) (continuous lines) and via a first-order Suzuki-Trotter evolution of the illustrated circuits. In the latter, we have explicitly included the phononic mode as in Eq. (9), truncating at the eighth level. The corresponding fidelity between the exact and the digitally simulated state is also shown. The time steps used for the Suzuki-Trotter evolution are indicated in the figures. In all the simulations, we set $m = g^2$.
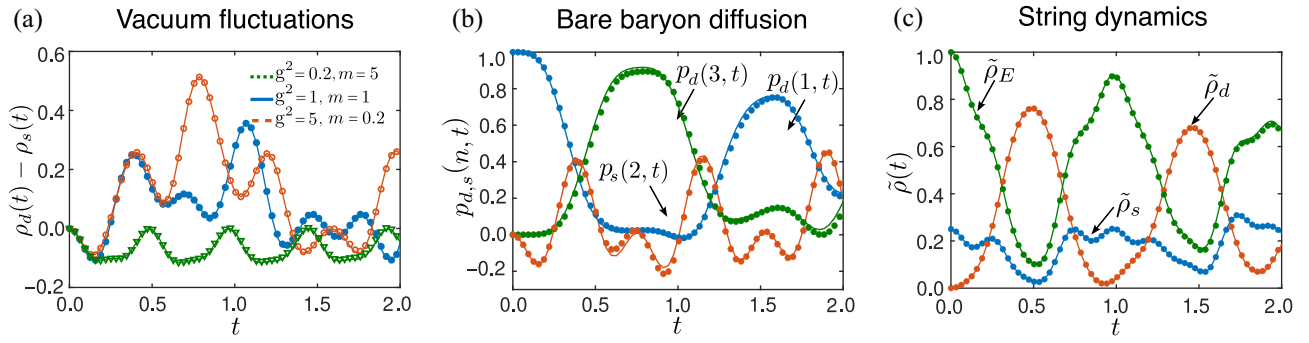
FIG. 5. Reproducing the model phenomenology. (a) The difference between the double- and single-particle-occupancy densities as a function of time for a lattice with $N = 3$ sites, considering various mass-coupling values as depicted in the figure. (b) The bare-baryon diffusion, analyzed for a lattice with $N = 3$ sites and $g^2 = m = 0.5$. The probabilities of double occupancy for the first and third atoms, denoted as $p_d(1, t)$ and $p_d(3, t)$, along with the single-occupancy probability for the second atom, denoted as $p_s(2, t)$, are studied over time. The initial condition involves a bare antibaryon excited in the first site. (c) The electric field, as well as the single- and double-occupancy string densities, plotted over time for a lattice comprising $N = 4$ sites with $g^2 = m = 5$. The string is initially excited within the sites $n = 1$–4. In all plots, the continuous lines represent the exact evolution of the model given in Eq. (6), while the discrete points correspond to the first-order Suzuki-Trotter evolution, with time step $dt = 0.01\pi$, performed using Eq. (9), which includes eight levels of the phononic mode.

for a string initially spanning the entire lattice. As in Fig. 3(c)(iii), we set the string energy to be in resonance with bare-meson and -baryon production. This tuning leads to pronounced oscillations in the quark and electric field densities, serving as indicators of the resonant excitations of bare mesons and baryons.

B. Link-parity preservation and postselection

As discussed in Sec. II, the employed rishon representation introduces an extra $\mathbb{Z}_2$ symmetry, which we set to an even number of rishons per link. While this symmetry is maintained throughout the Hamiltonian evolution, it may be compromised in actual simulations due to experimental errors leading to leakage from this subspace. These errors can be compensated in postselection by rejecting states that violate the symmetry, leading to a potentially significant reduction in simulation errors.

To select which data to retain, we make use of the parity matrices $\hat{D}^{(L)}$ and $\hat{D}^{(R)}$ defined in Table II, which ensures the link fermion-parity selection rule. When applied jointly to two neighboring sites, these operators yield a positive outcome if the link maintains the correct rishon parity and a negative outcome if the link deviates from the correct parity sector. Specifically, $\hat{D}_n^{(L)}\hat{D}_{n+1}^{(R)}|\Psi_{\text{phys}}\rangle = |\Psi_{\text{phys}}\rangle$ and $\hat{D}_n^{(L)}\hat{D}_{n+1}^{(R)}|\Psi_{\text{unphys}}\rangle = -|\Psi_{\text{unphys}}\rangle$, where $|\Psi_{\text{phys}}\rangle$ and $|\Psi_{\text{unphys}}\rangle$ represent the physical and unphysical states, respectively. These operators establish a truth table that facilitates the postselection of measurements conforming to the rishon parity.

We propose two different schemes for postselecting the data, based respectively on destructive and nondestructive measurements. The first exploits the truth table established by the parity operators to determine which states to retain

at the end of the simulation. This selection relies solely on the analysis of the qudit populations at each site, rejecting configurations involving adjacent unphysical states—those with just a single rishon on the link. However, it is important to note that this procedure does not entirely eliminate the possibility that, in previous time steps, the system may have exited the correct parity sector and returned to it afterward. Nevertheless, it serves as a filter and, since it only requires the qudit populations for each time step during the readout, it does not incur additional computational costs. The second protocol exploits an ancilla qubit to conduct state-preserving measurements. This approach offers the advantage of continuously monitoring the rishon parity during the time evolution but demands higher resources. The details of this scheme are discussed in Appendix D.

Another quantity that can be exploited to filter the data in postselection is the total baryon number $\hat{N}_b$, as defined in Sec. II A. This quantity is conserved by the dynamical evolution of the Hamiltonian given in Eq. (6). Any population configuration signaling deviations of this quantity from the initial setting of the simulation indicates the occurrence of an error in the evolution and the corresponding data should be rejected. Also, for this quantity, it is possible to design a nondestructive-measurement scheme to monitor possible deviations during the simulation. Unlike the link-parity protocol, this approach requires the utilization of an ancilla qutrit instead of a qubit (see Appendix D).

VI. EXPERIMENTAL CONSIDERATIONS

In this section, we explore the experimental challenges associated with realizing a quantum digital simulation. Several sources of error can impact the accuracy and effectiveness of the simulation. These include deviations from

the Lamb-Dicke regime and the rotating-wave approximation, motional heating, and magnetic field fluctuations [79,86,87]. Another significant hurdle is the implementation of the generalized MS gates via simultaneously driving multiple transitions. Achieving the correct target operation requires the precise calibration of many (linear in the number of transitions) coupled control parameters. Most notably, optical Stark shifts are induced by each laser tone [88,89], which creates an additional layer of complexity. In the following, we discuss some of these experimental challenges, which must be overcome for the successful experimental realization of the proposed quantum digital simulation.

A. Magnetic field fluctuations

To evaluate the impact of external magnetic field fluctuations, we have assumed infinitely correlated noise in time and space: throughout each single realization of the dynamics, the magnetic field $\mathcal{B}^z$ perceived by the ion qudits is constant and uniform. Therefore, the produced Zeeman shifts correspond to $\hat{H}_{Z0} = -\mathcal{B}^z \sum_n \hat{\mathbf{m}}_n^z$ with the magnetic dipole operator

$$\hat{\mathbf{m}}^z = \frac{1}{2}\begin{pmatrix} -3\mu_D & & & & & \\ & -\mu_D & & & & \\ & & -\mu_S & & & \\ & & & \mu_S & & \\ & & & & \mu_D & \\ & & & & & 3\mu_D \end{pmatrix},$$

(22)

where we consider a ratio $w = \mu_D/\mu_S \approx 0.6$ between the magnetic moments of the $D_{5/2}$ and the $S_{1/2}$ spin orbitals, compatible with Ref. [69]. Once we express this Hamiltonian shift in natural units, just as we did for the model Hamiltonian in Eq. (6), we can similarly identify a magnetic field realization via the dimensionless parameter $b = ((2\sqrt{2}a_0\mu_s)/c\hbar)\mathcal{B}^z$. Then, the rescaled (dimensionless) Hamiltonian $\hat{H}_Z = ((4\sqrt{2}a_0)/c\hbar)\hat{H}_{Z0}$ simply reads $\hat{H}_Z = -b\sum_n \hat{F}_n$, with

$$\hat{F}_n = \text{diag}(-3w, -w, -1, 1, w, 3w),$$ (23)

and we have incorporated the magnetic fluctuations Hamiltonian into the Suzuki-Trotter evolution of the Dirac vacuum depicted in Fig. 4(a). We have averaged over 100 realizations of time evolution, while randomly choosing in each realization r the (static uniform) rescaled magnetic coupling b_r from a uniform (flat) distribution within the interval $b_r \in [-\Delta b, \Delta b]$. For a comparative analysis with the exact evolution, we have computed the state fidelity, $\mathcal{F}(\tilde{t})$, at the time $\tilde{t}$, corresponding to the initial peak in the particle density observed in Fig. 4(a). This fidelity is shown in Fig. 6(a) as a function of the strength of the magnetic field fluctuations, Δb, for both first- and second-order
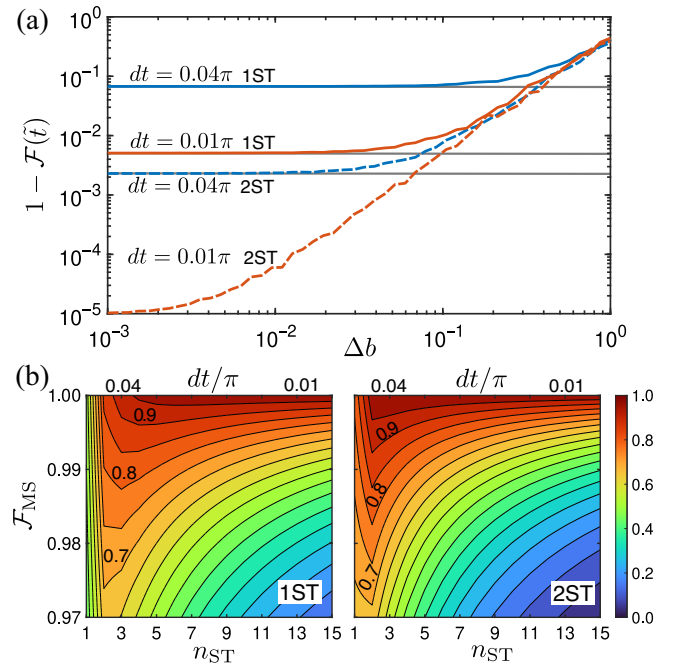

FIG. 6. Error estimation. (a) The state infidelity calculated with respect to the expected state at time $\tilde{t} = 0.377$ and the digitally simulated one as a function of the strength of the magnetic field fluctuations for the same configuration as in Fig. 4(a). The results have been obtained using the first scheme given in Fig. 4(a) and the continuous and dashed lines represent, respectively, the results obtained with a first- (ST1) and second-order (ST2) Suzuki-Trotter evolution. The gray lines indicate the ideal performance obtained in the absence of a magnetic field. We consider the same Suzuki-Trotter time steps as in Fig. 4, which require $n_{ST} = 12$ and $n_{ST} = 3$ steps, respectively, to reach $\tilde{t}$. (b) The estimation of the success probability of reaching the peak in the particle density at $\tilde{t} = 0.377$ versus the number of Suzuki-Trotter steps and the fidelity of a single generalized MS gate. The left and right panels are obtained, respectively, for the first- and second-order Suzuki-Trotter evolution.

(see Appendix C) Suzuki-Trotter evolutions, considering the same Trotter steps as in Fig. 4. The figure demonstrates that the fidelity is not significantly impacted for magnetic fluctuations inducing level shifts up to 10% of the particle hopping rate, set by $(\eta\Omega)^2/(2|\nu - \delta|)$ in the digital simulation. For expected hopping rates on the order of 0.1–1 kHz, this implies a requirement for magnetic field fluctuations to be maintained below the nanotesla threshold. Achieving this level of precision can be realized with current magnetic shielding techniques [90]. Another strategy that can be employed to reduce magnetic field fluctuations relies on performing a dynamical decoupling scheme [91,92]. In our case, this could be realized by applying two consecutive Suzuki-Trotter steps: the first with the current encoding and the second with a locally dressed basis (see Appendix E) rotated to acquire an opposite magnetic shift. Other schemes to perform dynamical decoupling of qudits,

albeit in different ion species, have recently been proposed [60,93]. Nevertheless, the main limitations for our proposal currently rely on intrinsic gate errors and pulse calibration, which we address in Sec. VI B.

B. Impact of other errors in the simulation

To make an agnostic estimation of the impact of other sources of error in the digital simulation, we assume that a single generalized two-qudit MS gate occurs with a finite fidelity $\mathcal{F}_{MS}$. If we neglect errors coming from single-qudit operations, which are performed with high precision, the overall performance of the simulation at a given time $t = n_{ST}dt$ can be estimated by the success probability

$$\mathcal{P}(t) = \mathcal{F}(t)[\mathcal{F}_{MS}]^{N_{gates}}, \tag{24}$$

where the total number of gates N_{gates} is defined in Eq. (21). In Fig. 6(b), we plot this success probability as a function of different values of the two-qudit gate fidelity and of the number of Suzuki-Trotter steps necessary to reach, as before, the peak of the particle-density creation at time $\tilde{t}$. In particular, we compare the results obtained with a first- and a second-order Suzuki-Trotter evolution, with the latter having $\mathcal{D} = 6$ circuit depth (see Appendix C). This estimation shows that with a two-qudit gate fidelity of the order of $\mathcal{F}_{MS} \gtrsim 0.99$, it is possible to obtain a success probability, $\mathcal{P} \sim 90\%$, sufficient for probing the dynamics of the model. Such two-qudit gate fidelities are achievable under the assumption that the errors associated with each transition are independent of each other. With this assumption, the overall error grows linearly with the number of transitions with respect to the standard MS qubit gate infidelity, which, according to the state of the art, can reach values of the order of 0.2% [94]. However, in the actual implementation, the generalized MS gate performance will depend on the accumulated errors coming from each driven transition, which generically are mutually dependent. The final gate fidelity then will rely on an optimal calibration process, as discussed in Sec. VI C.

C. Calibration challenges

Using multiple driving fields, even a standard qubit MS gate requires the calibration of four control parameters. In contrast to local gates, these control parameters are nonlinearly correlated and thus cannot be calibrated independently. As an example, consider a bichromatic light field, symmetrically detuned from an optical transition, as described in Sec. III. Changing the amplitude of one of the two laser tones nonlinearly shifts the transition frequency, which in turn changes the effective detuning and thus the coupling strength of the other tone. Moreover, due to the multilevel structure of the ion, these Stark shifts are different for each of the optical transitions. For a qubit MS gate, calibration typically involves four control parameters

that can be calibrated iteratively or in an automated fashion using Bayesian techniques [95].

For generalized MS gates, as discussed in Sec. III, the situation becomes significantly more difficult. Not only does a change in one parameter affect the entangling dynamics between the two states connected by the addressed transition but it now also affects the dynamics of states coupled by a simultaneously driven transition. While manual calibration of such a coupled multiparameter landscape seems very challenging, Bayesian parameter-estimation techniques might be extendable to this scenario, given a suitable cost function. Notably, the second approach discussed in Sec. III mediates these challenges, since it requires simultaneous driving only on disjoint transitions. This makes it possible to reduce the coupling between the parameters and precalibrate the operations on the two transitions independently to a large extent.

Finally, we observe that a further difficulty for the calibration process comes from the fact that the two-qudit gates presented in Sec. III require us to drive two different sets of transitions on the two ions n and $n + 1$. This issue can be solved by applying a rotation of the local dressed basis via unitary transformations, as discussed in Appendix E.

VII. CONCLUSIONS AND OUTLOOK

In summary, we have considered a Yang-Mills SU(2) 1D lattice gauge theory with dynamically coupled matter truncated at the lowest levels exhibiting nontrivial dynamics and non-Abelian features. We have introduced a compact rishon representation, embedding local gauge and fermionic degrees of freedom within a dimension-six Hilbert space, which has a natural encoding onto a qudit quantum processor based on $^{40}Ca^+$ trapped ions. We have presented three different schemes relying on entangling gates based, respectively, on a single, double disjoint, and four simultaneously driven transitions per ion. Relevantly, for the latter, we have demonstrated that an efficient digital quantum simulation of the model can be accomplished with a notably short circuit depth. This result is facilitated by harnessing the computational advantages inherent in qudits and is based on the efficacy of generalized MS gates. Note that, as also pointed out in other works [71–74], just the simple encoding of the model into qudits already brings substantial advantages with respect to qubit-based quantum digital simulations, which usually require larger computation resources and circuit depth and the capability of engineering long-range and/or three-or-more-body interactions [27,60,63,96–99].

The proposed qudit-encoding scheme, based on the local gauge-matter dressed basis, can be generalized to higher representations, symmetries, and dimensions. The most straightforward extensions consist of including the

$j = 1$ spin shell of the gauge field in the chromoelectric basis, which is achieved by employing a local dressed basis of total dimension $d = 10$ [50]. Similarly, an analogous (1+1)D SU(3) Yang-Mills model [truncated to the smallest nontrivial representations $(1, 0)$ and $(0, 1)$ for the gauge field], the phenomenology of which is closer to QCD such as three-quark baryons, can be achieved with a local dressed basis of dimension $d = 12$ [51]. Considering higher spatial dimensions, the non-Abelian rishon representation can be applied to describe a $j = 1/2$ truncated (2+1)D SU(2) model without dynamical matter (pure theory), with a local dressed basis of dimension $d = 9$ [50]. The major challenge in this case would come from the four-body plaquette term associated with the magnetic field. Such interaction could be decomposed into a series of two-qudit gates, as proposed in Ref. [71], or by exploiting four-body ion interactions [100,101]. All these extensions are within the state-of-the-art development with ion qudits, where full single-qudit control of 13-level trapped-ion qudits made of ^{137}Ba$^+$ has recently been demonstrated [70]. Further extensions could be envisioned by exploiting qudits with larger dimensions, such as those encoded in metastable states of ion isotopes with nuclear spin [102] and in circular levels of Rydberg atoms [65,66]. In conclusion, this proposal provides an experimentally feasible and potentially scalable pathway for observing non-Abelian lattice gauge phenomena, such as those from high-energy physics or emerging in condensed-matter models, in currently available qudit quantum processors.

The views and opinions expressed are, however, those of the authors only and do not necessarily reflect those of the European Union or the European Climate, Infrastructure and Environment Executive Agency (CINEA). Neither the European Union nor the granting authority can be held responsible for them.

APPENDIX A: RISHON REPRESENTATION

Once the hardcore-gluon approximation is adopted, the parallel transporter $\hat{U}^{ab}$ reads, in the chromoelectric five-dimensional basis of the gauge-field space [81],

$$\hat{U}^{ab} = \frac{1}{\sqrt{2}} \begin{pmatrix} 0 & +\delta_{ar}\delta_{bg} & -\delta_{ar}\delta_{br} & +\delta_{ag}\delta_{bg} & -\delta_{ag}\delta_{br} \\ -\delta_{ag}\delta_{br} & 0 & & & \\ -\delta_{ag}\delta_{bg} & & 0 & & \\ +\delta_{ar}\delta_{br} & & & 0 & \\ +\delta_{ar}\delta_{bg} & & & & 0 \end{pmatrix}. \quad \text{(A1)}$$

Here, we briefly decompose it as a pair of exotic fermion operators, each one acting on a suborbital (rishon). First, we need a practical strategy to define exotic fermion operators: a valid fermionic operator has a local action $\tilde{F}$ that inverts a local parity $\hat{P} = \hat{P}^\dagger = \hat{P}^{-1}$, so that $\{\hat{P}, \tilde{F}\} = 0$. In analogy to the Jordan-Wigner transformation, the global action of the fermion operator $\hat{F}$ is the string

$$\hat{F}_n = \dots \hat{P}_{n-2} \otimes \hat{P}_{n-1} \otimes (\tilde{F})_n \otimes \mathbb{1}_{n+1} \otimes \mathbb{1}_{n+2} \dots, \quad \text{(A2)}$$

in contrast to a boson $\hat{B}$ (or spin) global action, which instead reads

$$\hat{B}_n = \dots \mathbb{1}_{n-2} \otimes \mathbb{1}_{n-1} \otimes (\tilde{B})_n \otimes \mathbb{1}_{n+1} \otimes \mathbb{1}_{n+2} \dots. \quad \text{(A3)}$$

This prescription ensures that any two fermion operators on different modes anticommute as they should: $\{\hat{F}_n, \hat{F}_{'\neq n}\} = \{\hat{F}_n, \hat{\psi}_{n'\neq n}^{(\dagger)}\} = 0$. In this formalism, it is straightforward to define a Dirac fermion lattice field,

$$\hat{\psi}_{\text{Dirac}} = \begin{pmatrix} 0 & 1 \\ 0 & 0 \end{pmatrix}_F, \qquad \hat{P}_\psi = \begin{pmatrix} +1 & 0 \\ 0 & -1 \end{pmatrix}, \quad \text{(A4)}$$

as well as a Majorana one,

$$\hat{c}_{\text{Majo}} = \begin{pmatrix} 0 & 1 \\ 1 & 0 \end{pmatrix}_F, \qquad \hat{P}_c = \begin{pmatrix} +1 & 0 \\ 0 & -1 \end{pmatrix}, \quad \text{(A5)}$$

where the subscript "F" specifies that the operator is meant to be understood as a fermion, i.e., that this global action has a parity string attached, as in Eq. (A2).

We can then define a pair of exotic fermion operators for the rishon space, written in the basis $\{|0\rangle, |r\rangle, |g\rangle\}$, namely,

$$
\hat{\zeta}^{\mathrm{r}} = \left(\begin{array}{c|cc} 0 & 1 & 0 \\ \hline 0 & 0 & 0 \\ 1 & 0 & 0 \end{array}\right)_F, \qquad \hat{\zeta}^{\mathrm{g}} = \left(\begin{array}{c|cc} 0 & 0 & 1 \\ \hline -1 & 0 & 0 \\ 0 & 0 & 0 \end{array}\right)_F,
$$
(A6)

with the corresponding local fermion parity

$$
\hat{P}_\zeta = \left(\begin{array}{c|cc} 1 & 0 & 0 \\ \hline 0 & -1 & 0 \\ 0 & 0 & -1 \end{array}\right).
$$
(A7)

One can then check that the parallel transporter can be decomposed as

$$
\hat{U}^{ab}_{n,n+1} = \frac{1}{\sqrt{2}} \left(\hat{\zeta}^a_n\right)_L \left(\hat{\zeta}^b_{n+1}\right)^\dagger_R.
$$
(A8)

Performing such a decomposition greatly simplifies the covariant hopping from the lattice Yang-Mills Hamiltonian, specifically,

$$
\begin{aligned}
\hat{H}_{\mathrm{hop}} &= \frac{c\hbar}{2a_0} \sum_n \sum_{a,b=\mathrm{r,g}} \left[-i\hat{\psi}^\dagger_{na} \hat{U}^{ab}_{n,n+1} \hat{\psi}_{n+1b} + \mathrm{H.c.}\right] \\
&= \frac{\sqrt{2}c\hbar}{4a_0} \sum_n \sum_{a,b=\mathrm{r,g}} \left[-i\hat{\psi}^\dagger_{na} \left(\hat{\zeta}^a_n\right)_L \left(\hat{\zeta}^b_{n+1}\right)^\dagger_R \right. \\
&\qquad\qquad \left. \times \hat{\psi}_{n+1b} + \mathrm{H.c.}\right] \\
&= \frac{\sqrt{2}c\hbar}{4a_0} \sum_n \left[\hat{Q}^\dagger_{Ln} \hat{Q}_{R,n+1} + \hat{Q}_{Ln} \hat{Q}^\dagger_{R,n+1}\right],
\end{aligned}
$$
(A9)

where the operators $\hat{Q}_{L,n} = \sum_{a=\mathrm{r,g}} \left(\hat{\zeta}^a_n\right)^\dagger_L \hat{\psi}_{na}$ and $\hat{Q}_{R,n} = -i\sum_{a=\mathrm{r,g}} \left(\hat{\zeta}^a_n\right)^\dagger_R \hat{\psi}_{na}$ are explicitly gauge invariant and genuinely local (preserving the fermion parity on the dressed site). On the six-dimensional logical basis for the dressed site, these matrices read as reported in Table III. They are not Hermitian, however, so they still need to be manipulated for quantum simulation with trapped ions. Therefore, we substitute

$$
\begin{aligned}
\hat{A}^{(1)} &= \hat{Q}_L + \hat{Q}^\dagger_L, & \hat{B}^{(1)} &= \hat{Q}_R + \hat{Q}^\dagger_R, \\
\hat{A}^{(2)} &= i(\hat{Q}_L - \hat{Q}^\dagger_L), & \hat{B}^{(2)} &= i(\hat{Q}_R - \hat{Q}^\dagger_R),
\end{aligned}
$$
(A10)

where we have defined four Hermitian operators. Now, by noting that $\hat{A}^{(1)} \otimes \hat{B}^{(1)} + \hat{A}^{(2)} \otimes \hat{B}^{(2)}$ is equal to $2\hat{Q}^\dagger_L \otimes$

TABLE III. The effective model matrices $\hat{Q}_L$ and $\hat{Q}_R$ written in the gauge-invariant canonical basis of the dressed site.

$\hat{Q}_L$		$\hat{Q}_R$
$\begin{pmatrix} 0 & & \sqrt{2} & & & \\ & 0 & & 1 & & \\ & & 0 & & & 1 \\ & & & 0 & \sqrt{2} & \\ & & & & 0 & \\ & & & & & 0 \end{pmatrix}$	$-i$	$\begin{pmatrix} 0 & & \sqrt{2} & & & \\ & 0 & & 1 & & \\ & & 0 & & \sqrt{2} & \\ & & & 0 & & 1 \\ & & & & 0 & \\ & & & & & 0 \end{pmatrix}$

$\hat{Q}_R + 2\hat{Q}_L \otimes \hat{Q}^\dagger_R$, we can conclude that

$$
\hat{H}_{\mathrm{hop}} = \frac{\sqrt{2}c\hbar}{8a_0} \sum_n \left[\hat{A}^{(1)}_n \hat{B}^{(1)}_{n+1} + \hat{A}^{(2)}_n \hat{B}^{(2)}_{n+1}\right],
$$
(A11)

which is the expression for the nearest-neighbor term that appears in the main text.

Regarding the chromoelectric energy density, we can split the energy contribution half-half to each rishon (the quadratic Casimir eigenvalue must be the same on the two halves due to the link law). Basically,

$$
\hat{H}_{\mathrm{elec}} = g^2 \frac{c\hbar}{4a_0} \sum_n \left(|\hat{\mathbf{R}}_{n,n+1}|^2 + |\hat{\mathbf{L}}_{n,n+1}|^2\right)
$$
(A12)

but the quadratic Casimir on the rishon space simply reads

$$
|\hat{\mathbf{L}}|^2 \backslash |\hat{\mathbf{R}}|^2 = \left(\begin{array}{c|cc} 0 & 0 & 0 \\ \hline 0 & 3/4 & 0 \\ 0 & 0 & 3/4 \end{array}\right) = \frac{3}{4}\hat{K}.
$$
(A13)

Therefore, in conclusion,

$$
\hat{H}_{\mathrm{elec}} = g^2 \frac{3c\hbar}{16a_0} \sum_n \left(\hat{K}_{L,n} + \hat{K}_{R,n}\right)
$$
(A14)

and the sum $\hat{K}_L + \hat{K}_R$ on a dressed site is exactly the operator $\hat{C}$.

APPENDIX B: PERTURBATIVE MODEL IN THE STRONG-COUPLING LIMIT

In the strong-coupling limit, $g \gg 1$, the excitation of the link becomes energetically costly and the field can be adiabatically eliminated. The description of the model is then reduced to the bare-matter states $|1\rangle$ and $|5\rangle$, which we rename $|\uparrow\rangle = |5\rangle$ and $|\downarrow\rangle = |1\rangle$. A simple hopping process between these two states can be obtained in perturbation theory and leads to the following Heisenberg model

in a staggered magnetic field:

$$\hat{H}_{\text{Heis}} = -\frac{4}{\bar{g}^2} \sum_n \hat{\boldsymbol{\sigma}}_n \cdot \hat{\boldsymbol{\sigma}}_{n+1} + m \sum_n (-1)^n \hat{\sigma}_n^z, \quad \text{(B1)}$$

where $\bar{g}^2 = g^2 + m$ and $\hat{\boldsymbol{\sigma}} = (\hat{\sigma}^x, \hat{\sigma}^y, \hat{\sigma}^z)$. Within this model, the Dirac vacuum corresponds to the antiferromagnetic ground state. Assuming that we initially flip a single spin out of this vacuum, corresponding to the excitation of a bare baryon in the original model, a second-order hopping process occurs in the limit of $\bar{g}^2 m \gg 1$. This process gives rise to the following tight-binding Hamiltonian:

$$\hat{H}_{\text{eff}} = J_{\text{eff}} \sum_n \left(\hat{\sigma}_n^+ \hat{\sigma}_{n+1}^- + \hat{\sigma}_n^- \hat{\sigma}_{n+1}^+ \right), \quad \text{(B2)}$$

with hopping rate $J_{\text{eff}} = 16/\bar{g}^4 m$, which describes the diffusion of bare baryons at a speed $v_g = 2J_{\text{eff}}$. This result has been obtained in a two-step perturbation process. A more precise effective description can be obtained by performing directly a fourth-order perturbation theory in the limit $g, m \gg J$, considering explicitly the two hopping paths accessible to an initially excited baryon:

$$
\begin{array}{llll}
|5\rangle|5\rangle|1\rangle & E = 0, & |5\rangle|5\rangle|1\rangle & E = 0, \\
|5\rangle|4\rangle|3\rangle & E = 2m + 2g^2, & |5\rangle|4\rangle|3\rangle & E = 2m + 2g^2, \\
|5\rangle|1\rangle|5\rangle & E = 4m, & |4\rangle|6\rangle|3\rangle & E = 4g^2, \\
|4\rangle|3\rangle|5\rangle & E = 2m + 2g^2, & |4\rangle|3\rangle|5\rangle & E = 2m + 2g^2, \\
|1\rangle|5\rangle|5\rangle & E = 0, & |1\rangle|5\rangle|5\rangle & E = 0,
\end{array}
$$
$$\text{(B3)}$$

where for each state, we have indicated the bare energy cost. Performing an adiabatic elimination at the fourth

order, we finally obtain the following effective coupling rate:

$$J_{\text{eff}} = \frac{16}{m\bar{g}^4} + \frac{8}{g^2 \bar{g}^4}, \quad \text{(B4)}$$

which reduces to the one previously derived in the limit of $g \gg m$.

APPENDIX C: SECOND-ORDER SUZUKI-TROTTER DECOMPOSITION

In the main text, we have shown how employing a second-order Suzuki-Trotter decomposition can be beneficial for the simulation, even if it implies a slightly larger circuit depth. The unit-cells circuit is presented in Fig. 7(a). The first and last gates can be merged in one during the evolution; thus the circuit depth is $\mathcal{D} = 6$. To ensure in this scheme a reduced population of the phonic mode, we set $d\bar{t} = 4\pi/|\nu - \delta|$ for all the applied gates. In Fig. 7(a), we show the performance of this scheme, again considering the particle creation out of the Dirac vacuum and the corresponding state fidelity in time, comparing the results obtained with the first- and second-order Suzuki-Trotter decompositions. The plot shows a clear improvement of the simulation performance due to the reduced Suzuki-Trotter error.

APPENDIX D: NONDESTRUCTIVE-MEASUREMENT ERROR-DETECTION PROTOCOL

1. Link symmetry

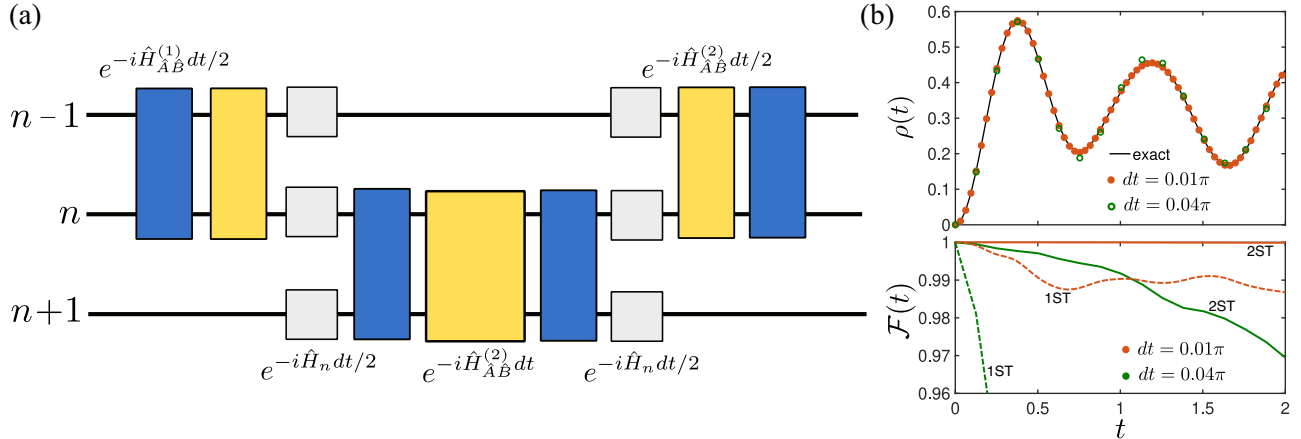The link-parity-preservation protocol presented in the main text to preserve the link symmetry has the

FIG. 7. Second-order Suzuki-Trotter decomposition. (a) The unit-cell circuit for the second-order Suzuki-Trotter decomposition. The first and last gates can be combined in one of duration dt, leading to a circuit depth of $\mathcal{D} = 6$. (b) The particle density as function of time for the Dirac vacuum with $N = 3$ lattice sites. The continuous line has been obtained with the exact model, while the dots have been obtained via the second-order Suzuki-Trotter (ST2) evolution of the illustrated circuit, using the time steps indicated in the figure. Below is shown the corresponding fidelity between the exact and the digitally simulated state comparing the results of the first- (dashed line) and second-order (continuous line) Suzuki-Trotter decompositions. For the ST2, we have included the phononic mode truncating at the eighth level.

disadvantage of relying on destructive measurements. As an alternative scheme, here we propose a strategy based on state-preserving measurements. This approach offers the advantage of continuously monitoring (and quantum Zeno protecting) rishon parity during the evolution of the system. The core concept involves the utilization of an ancilla qubit per qudit pair, which may also be represented by an unused qudit level, to conduct state-preserving measurements. Focusing on two adjacent sites, denoted as n and $n+1$, let us consider a scenario in which, during the evolution of the system, the state tends to leak out of the parity sector due to experimental errors. The generic form of the state of the two sites then reads

$$|\psi\rangle = \sum_r a_r|\psi_{\text{phys}}\rangle_r + \sum_r b_r|\psi_{\text{unphys}}\rangle_r, \qquad \text{(D1)}$$

where $|\psi_{\text{phys}}\rangle_r$ and $|\psi_{\text{unphys}}\rangle_r$ represent states living in the even- and odd-symmetry sectors. Here, for simplicity, we are assuming a coherent superposition between the two, but an analogous argument works for a generic statistical mixture. To nondestructively measure parity, we employ a hybrid version of the controlled-exchange (CEX$_c$) gate, already implemented in the trapped-ion-qudit quantum processor [69]:

$$\text{CEX}_c = \begin{cases} |s,\uparrow\rangle \leftrightarrow |s,\downarrow\rangle, & \text{if } s = c, \\ |s,k\rangle \rightarrow |s,k\rangle, & \text{if } s \neq c, \end{cases} \qquad \text{(D2)}$$

where $|s,k\rangle$ represents the product state between the qudit and the qubit. This gate flips the state of the ancilla qubit if the qudit is in the state $|c\rangle$ and retains the state of the qubit if the qudit is in any other state. We initialize the ancilla in the state $|\downarrow\rangle_a$ and apply a sequence of CEX$_c$ gates on each qudit. The choice of the state of the $|c\rangle$ qudit corresponds to the negative values of the two parity operators given in Table II associated with each qudit pair, as illustrated in Fig. 8(a). A similar sequence is then applied separately at the first and last qudits of the chain to ensure that the parity remains fixed at the boundaries. This process results in the following state for two adjacent sites:

$$|\psi\rangle = \sum_r a_r|\psi_{\text{phys}}\rangle_r|\downarrow\rangle_a + \sum_r b_r|\psi_{\text{unphys}}\rangle_r|\uparrow\rangle_a. \quad \text{(D3)}$$

With this procedure, we can monitor the evolution of the state at each time step. In particular, if the ancilla qubit remains in its initial state, we can be confident that the evolution has occurred within the correct symmetry sector. However, if the ancilla qubit flips, indicating a deviation, it suggests a leakage into the odd-symmetry sector.

Note that if we neglect the possibility of having more than one qudit error in the chain within a given time step, this nondestructive measurement of the link-parity errors is capable of detecting all possible single-qudit state flips
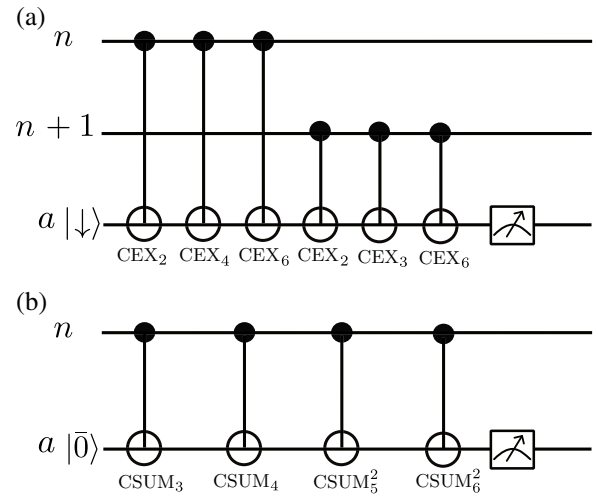

FIG. 8. The (a) parity and (b) baryon-number check circuits to maintain the evolution in the correct parity or baryon sector. In the scheme presented in (a), an ancilla qubit is employed per each pair of qudits, while in (b), the same ancilla qutrit is used for all of the chain.

besides the ones maintaining the same link parity, i.e., $|1\rangle \leftrightarrow |5\rangle$ and $|2\rangle \leftrightarrow |6\rangle$. To also detect this kind of error, in Sec. D 2 we propose a nondestructive scheme to monitor deviations in the baryon number of the chain.

2. Baryon number

Let us assume, in the following, that our qudit quantum processor is affected only by single-qudit errors in each time step. Such errors can induce a modification of the total baryon number $\hat{N}_b = \frac{1}{2}\sum_n(\hat{M}_n - 1)$, which for a single-qudit flip can vary by an half integer or by an integer, i.e., $\Delta\hat{N}_b = \pm\frac{1}{2}, \pm 1$. Deviation in this quantity can be monitored during the evolution by using an ancilla qutrit for the entire chain spanned by the basis set $|t\rangle_a = |\bar{0}\rangle_a, |\bar{1}\rangle_a, |\bar{2}\rangle_a$, with the two upper states counting for half integer and integer deviations, respectively. In this case, we employ the controlled-SUM (CSUM$_c$) gate, which is available in the trapped-ion-qudit quantum processor [69]:

$$\text{CSUM}_c = \begin{cases} |s,t\rangle \leftrightarrow |s,t \oplus 1\rangle, & \text{if } s = c, \\ |s,k\rangle \rightarrow |s,k\rangle, & \text{if } s \neq c, \end{cases} \qquad \text{(D4)}$$

where $\oplus$ denotes addition modulo 3 and where $|s,k\rangle$ represents the product state between the qudit and the qutrit. We initialize the qutrit ancilla in the state $|\bar{0}\rangle_a$ and then apply to each qudit the sequence of gates CSUM$_3$, CSUM$_4$, CSUM$_5^2$, and CSUM$_6^2$ shown in Fig. 8(b). Here, the gates CSUM$_c^2$ perform the operation $|c,t\rangle \leftrightarrow |c,t \oplus 2\rangle$ if the qudit is in state c. With this scheme, if the ancilla qutrit at the end of the process takes a value different from $|\bar{0}\rangle$, a single-qudit flip has occurred. Importantly, the qudit flips not detectable from the link-parity symmetry, i.e.,

$|1\rangle \leftrightarrow |5\rangle$ and $|2\rangle \leftrightarrow |6\rangle$, are signaled by a qutrit readout $|t\rangle_a = |\bar{2}\rangle$. With this procedure, combined with the link-symmetry nondestructive measurement, all possible single-qudit symmetry violations can be detected at each time step.

APPENDIX E: LOCAL DRESSED BASIS ROTATION

The two-qudit gates discussed in Sec. III require us to drive two different set of transitions on the qudit of the two ions. This is not a fundamental problem *per se* but it can affect the complexity of the pulse-calibration process. A solution to this issue consists in performing a unitary transformation of the local dressed basis on just the even lattice sites, using the following unitary operator:

$$
\hat{V} = \begin{pmatrix} i & & & & & \\ & i & & & & \\ & & 0 & 1 & & \\ & & 1 & 0 & & \\ & & & & -i & \\ & & & & & -i \end{pmatrix}.
\tag{E1}
$$

This matrix transforms the operators of the model Eq. (6) according to

$$
\begin{aligned}
\hat{V}\hat{A}^{(k)}\hat{V}^{\dagger} &= -\hat{B}^{(k)}, \\
\hat{V}\hat{B}^{(k)}\hat{V}^{\dagger} &= \hat{A}^{(k)}, \\
\hat{V}\hat{M}\hat{V}^{\dagger} &= \hat{M}, \\
\hat{V}\hat{C}\hat{V}^{\dagger} &= \hat{C},
\end{aligned}
\tag{E2}
$$

with $k = 1, 2$. The Hamiltonian given in Eq. (6) than reads

$$
\begin{aligned}
\hat{H} = &\sum_{n \in \text{odd}} \left[\hat{A}_n^{(1)}\hat{A}_{n+1}^{(1)} + \hat{A}_n^{(2)}\hat{A}_{n+1}^{(2)} \right] \\
&- \sum_{n \in \text{even}} \left[\hat{B}_n^{(1)}\hat{B}_{n+1}^{(1)} + \hat{B}_n^{(2)}\hat{B}_{n+1}^{(2)} \right] \\
&+ m \sum_n (-1)^n \hat{M}_n + g^2 \sum_n \hat{C}_n.
\end{aligned}
\tag{E3}
$$

In this way, as required, the two-qudit gates necessary to implement the hopping terms always involve the same operator acting on the pair of qudits. This change of local basis should be applied before and after the sequence of four two-qudit gates presented in Fig. 4. To conclude the protocol, after having returned to the original basis, the single-qudit compensation operations [see Eq. (12)] can be applied as in the main text.

For the disjoint double-transition scheme, it is also possible to apply local transformations in order to have two-qudit gates involving the same operator on both qudits.

Compared to the full scheme, the same basis transformation cannot be applied for all of the gates but different single-qudit rotations should be applied on each site before and after each two-qudit gate. In particular, it is possible to reduce all the two-qudit gates to always be of the same form by using the unitary transformations

$$
\hat{V}_{\hat{\alpha}_q^{(k)}\hat{\alpha}_{q'}^{(k')}} \hat{\alpha}_q^{(k)} \hat{V}_{\hat{\alpha}_q^{(k)}\hat{\alpha}_{q'}^{(k')}}^{\dagger} = \hat{\alpha}_{q'}^{(k')},
\tag{E4}
$$

$$
\hat{V}_{\hat{\beta}_q^{(k)}\hat{\alpha}_{q'}^{(k')}} \hat{\beta}_q^{(k)} \hat{V}_{\hat{\beta}_q^{(k)}\hat{\alpha}_{q'}^{(k')}}^{\dagger} = \hat{\alpha}_{q'}^{(k')},
\tag{E5}
$$

with $k, q, k', q' = 1, 2$. Again, the single-qudit compensation matrices could be applied in a similar way how they are applied in the main text, at the end of the series of gates, when the local basis is transformed back to the original one.

---

[1] A. S. Kronfeld, Twenty-first century lattice gauge theory: Results from the quantum chromodynamics lagrangian, Annu. Rev. Nucl. Part. Sci. **62**, 265 (2012).

[2] E. Fradkin, *Field Theories of Condensed Matter Physics* (Cambridge University Press, 2013), 2nd ed.

[3] B. Zeng, X. Chen, D.-L. Zhou, and X.-G. Wen, *Quantum Information Meets Quantum Matter* (Springer, 2019).

[4] K. G. Wilson, Confinement of quarks, Phys. Rev. D **10**, 2445 (1974).

[5] J. Kogut and L. Susskind, Hamiltonian formulation of Wilson's lattice gauge theories, Phys. Rev. D **11**, 395 (1975).

[6] T. Banks, L. Susskind, and J. Kogut, Strong-coupling calculations of lattice gauge theories: $(1 + 1)$-dimensional exercises, Phys. Rev. D **13**, 1043 (1976).

[7] C. Gattringer and C. Lang, *Quantum Chromodynamics on the Lattice: An Introductory Presentation* (Springer Science & Business Media, 2009), Vol. 788.

[8] E. A. Calzetta and B.-L. B. Hu, in *Cambridge Monographs on Mathematical Physics* (Cambridge University Press, 2008).

[9] P. Silvi, E. Rico, T. Calarco, and S. Montangero, Lattice gauge tensor networks, New J. Phys. **16**, 103015 (2014).

[10] M. Dalmonte and S. Montangero, Lattice gauge theory simulations in the quantum information era, Contemp. Phys. **57**, 388 (2016).

[11] P. Silvi, F. Tschirsich, M. Gerster, J. Jünemann, D. Jaschke, M. Rizzi, and S. Montangero, The tensor networks anthology: Simulation techniques for many-body quantum lattice systems, SciPost Phys. Lect. Notes, 8 (2019).

[12] U.-J. Wiese, Ultracold quantum gases and lattice systems: Quantum simulation of lattice gauge theories, Ann. Phys. **525**, 777 (2013).

[13] M. C. Banuls, R. Blatt, J. Catani, A. Celi, J. I. Cirac, M. Dalmonte, L. Fallani, K. Jansen, M. Lewenstein, S. Montangero *et al.*, Simulating lattice gauge theories within quantum technologies, Eur. Phys. J. D **74**, 1 (2020).

[14] A. Di Meglio, K. Jansen, I. Tavernelli, C. Alexandrou, S. Arunachalam, C. W. Bauer, K. Borras, S. Carrazza, A. Crippa, V. Croft *et al.*, Quantum computing for high-energy physics: State of the art and challenges, PRX Quantum **5**, 037001 (2024).

[15] J. C. Halimeh, M. Aidelsburger, F. Grusdt, P. Hauke, and B. Yang, Cold-atom quantum simulators of gauge theories, arXiv:2310.12201.

[16] D. Banerjee, M. Dalmonte, M. Müller, E. Rico, P. Stebler, U.-J. Wiese, and P. Zoller, Atomic quantum simulation of dynamical gauge fields coupled to fermionic matter: From string breaking to evolution after a quench, Phys. Rev. Lett. **109**, 175302 (2012).

[17] E. Zohar, J. I. Cirac, and B. Reznik, Quantum simulations of lattice gauge theories using ultracold atoms in optical lattices, Rep. Prog. Phys. **79**, 014401 (2015).

[18] E. Zohar, A. Farace, B. Reznik, and J. I. Cirac, Digital lattice gauge theories, Phys. Rev. A **95**, 023604 (2017).

[19] S. Kühn, J. I. Cirac, and M.-C. Bañuls, Quantum simulation of the Schwinger model: A study of feasibility, Phys. Rev. A **90**, 042305 (2014).

[20] L. Tagliacozzo, A. Celi, A. Zamora, and M. Lewenstein, Optical Abelian lattice gauge theories, Ann. Phys. (NY) **330**, 160 (2013).

[21] L. Tagliacozzo, A. Celi, P. Orland, M. Mitchell, and M. Lewenstein, Simulation of non-Abelian gauge theories with optical lattices, Nat. Commun. **4**, 2615 (2013).

[22] B. Yang, H. Sun, R. Ott, H.-Y. Wang, T. V. Zache, J. C. Halimeh, Z.-S. Yuan, P. Hauke, and J.-W. Pan, Observation of gauge invariance in a 71-site Bose-Hubbard quantum simulator, Nature **587**, 392 (2020).

[23] J. C. Halimeh, L. Homeier, A. Bohrdt, and F. Grusdt, Spin exchange-enabled quantum simulator for large-scale non-Abelian gauge theories, arXiv:2305.06373.

[24] M. Aidelsburger, L. Barbiero, A. Bermudez, T. Chanda, A. Dauphin, D. González-Cuadra, P. R. Grzybowski, S. Hands, F. Jendrzejewski, J. Jünemann *et al.*, Cold atoms meet lattice gauge theory, Philos. Trans. R. Soc. A **380**, 20210064 (2022).

[25] D. Marcos, P. Rabl, E. Rico, and P. Zoller, Superconducting circuits for quantum simulation of dynamical gauge fields, Phys. Rev. Lett. **111**, 110504 (2013).

[26] A. Mezzacapo, E. Rico, C. Sabín, I. L. Egusquiza, L. Lamata, and E. Solano, Non-Abelian SU(2) lattice gauge theories in superconducting circuits, Phys. Rev. Lett. **115**, 240502 (2015).

[27] Y. Y. Atas, J. Zhang, R. Lewis, A. Jahanpour, J. F. Haase, and C. A. Muschik, SU(2) hadrons on a quantum computer via a variational approach, Nat. Commun. **12**, 6499 (2021).

[28] R. C. Farrell, M. Illa, A. N. Ciavarella, and M. J. Savage, Quantum simulations of hadron dynamics in the Schwinger model using 112 qubits, Phys. Rev. D **109**, 114510 (2024).

[29] P. Hauke, D. Marcos, M. Dalmonte, and P. Zoller, Quantum simulation of a lattice Schwinger model in a chain of trapped ions, Phys. Rev. X **3**, 041018 (2013).

[30] E. A. Martinez, C. A. Muschik, P. Schindler, D. Nigg, A. Erhard, M. Heyl, P. Hauke, M. Dalmonte, T. Monz, P. Zoller *et al.*, Real-time dynamics of lattice gauge theories with a few-qubit quantum computer, Nature **534**, 516 (2016).

[31] C. Muschik, M. Heyl, E. Martinez, T. Monz, P. Schindler, B. Vogell, M. Dalmonte, P. Hauke, R. Blatt, and P. Zoller, U(1) Wilson lattice gauge theories in digital quantum simulators, New J. Phys. **19**, 103020 (2017).

[32] N. H. Nguyen, M. C. Tran, Y. Zhu, A. M. Green, C. H. Alderete, Z. Davoudi, and N. M. Linke, Digital quantum simulation of the Schwinger model and symmetry protection with trapped ions, PRX Quantum **3**, 020324 (2022).

[33] Z. Davoudi, M. Hafezi, C. Monroe, G. Pagano, A. Seif, and A. Shaw, Towards analog quantum simulations of lattice gauge theories with trapped ions, Phys. Rev. Res. **2**, 023015 (2020).

[34] E. Rico, T. Pichler, M. Dalmonte, P. Zoller, and S. Montangero, Tensor networks for lattice gauge theories and atomic quantum simulation, Phys. Rev. Lett. **112**, 201601 (2014).

[35] T. Pichler, M. Dalmonte, E. Rico, P. Zoller, and S. Montangero, Real-time dynamics in U(1) lattice gauge theories with tensor networks, Phys. Rev. X **6**, 011023 (2016).

[36] E. Ercolessi, P. Facchi, G. Magnifico, S. Pascazio, and F. V. Pepe, Phase transitions in Z_n gauge models: Towards quantum simulations of the Schwinger-Weyl QED, Phys. Rev. D **98**, 074503 (2018).

[37] G. Magnifico, M. Dalmonte, P. Facchi, S. Pascazio, F. V. Pepe, and E. Ercolessi, Real time dynamics and confinement in the $\mathbb{Z}_n$ Schwinger-Weyl lattice model for $1+1$ QED, Quantum **4**, 281 (2020).

[38] W.-Y. Zhang, Y. Liu, Y. Cheng, M.-G. He, H.-Y. Wang, T.-Y. Wang, Z.-H. Zhu, G.-X. Su, Z.-Y. Zhou, Y.-G. Zheng *et al.*, Observation of microscopic confinement dynamics by a tunable topological θ-angle, arXiv:2306.11794.

[39] J. Mildenberger, W. Mruczkiewicz, J. C. Halimeh, Z. Jiang, and P. Hauke, Probing confinement in a $\mathbb{Z}_2$ lattice gauge theory on a quantum computer, arXiv:2203.08905.

[40] M. Rigobello, S. Notarnicola, G. Magnifico, and S. Montangero, Entanglement generation in $(1 + 1)$D QED scattering processes, Phys. Rev. D **104**, 114501 (2021).

[41] P. Emonts, A. Kelman, U. Borla, S. Moroz, S. Gazit, and E. Zohar, Finding the ground state of a lattice gauge theory with fermionic tensor networks: A $2 + 1$D $\mathbb{Z}_2$ demonstration, Phys. Rev. D **107**, 014505 (2023).

[42] L. Funcke, K. Jansen, and S. Kühn, Exploring the *CP*-violating Dashen phase in the Schwinger model with tensor networks, Phys. Rev. D **108**, 014504 (2023).

[43] T. Angelides, L. Funcke, K. Jansen, and S. Kühn, Computing the mass shift of Wilson and staggered fermions in the lattice Schwinger model with matrix product states, Phys. Rev. D **108**, 014516 (2023).

[44] R. Belyansky, S. Whitsitt, N. Mueller, A. Fahimniya, E. R. Bennewitz, Z. Davoudi, and A. V. Gorshkov, High-energy collision of quarks and mesons in the Schwinger model: From tensor networks to circuit QED, Phys. Rev. Lett. **132**, 091903 (2024).

[45] M. Kebrič, J. C. Halimeh, U. Schollwöck, and F. Grusdt, Confinement in $(1 + 1)$-dimensional $\mathbb{Z}_2$ lattice gauge theories at finite temperature, Phys. Rev. B **109**, 245110 (2024).

[46] A. Florio, A. Weichselbaum, S. Valgushev, and R. D. Pisarski, Mass gaps of a $\mathbb{Z}_3$ gauge theory with three fermion flavors in $1 + 1$ dimensions, Phys. Rev. D **110**, 045013 (2024).

[47] S. Kühn, E. Zohar, J. I. Cirac, and M. C. Bañuls, Non-Abelian string breaking phenomena with matrix product states, J. High Energy Phys. **2015**, 1 (2015).

[48] P. Silvi, E. Rico, M. Dalmonte, F. Tschirsch, and S. Montangero, Finite-density phase diagram of a $(1 + 1) - d$ non-Abelian lattice gauge theory with tensor networks, Quantum **1**, 9 (2017).

[49] M. C. Bañuls, K. Cichy, J. I. Cirac, K. Jansen, and S. Kühn, Efficient basis formulation for $(1 + 1)$-dimensional SU(2) lattice gauge theory: Spectral calculations with matrix product states, Phys. Rev. X **7**, 041046 (2017).

[50] G. Cataldi, G. Magnifico, P. Silvi, and S. Montangero, Simulating $(2 + 1)$D SU(2) Yang-Mills lattice gauge theory at finite density with tensor networks, Phys. Rev. Res. **6**, 033057 (2024).

[51] M. Rigobello, G. Magnifico, P. Silvi, and S. Montangero, Hadrons in $(1 + 1)$D Hamiltonian hardcore lattice QCD, arXiv:2308.04488.

[52] T. Hayata, Y. Hidaka, and K. Nishimura, Dense QCD2 with matrix product states, J. High Energy Phys. **2024**, 1 (2024).

[53] Z.-Y. Zhou, G.-X. Su, J. C. Halimeh, R. Ott, H. Sun, P. Hauke, B. Yang, Z.-S. Yuan, J. Berges, and J.-W. Pan, Thermalization dynamics of a gauge theory on a quantum simulator, Science **377**, 311 (2022).

[54] D. Paulson, L. Dellantonio, J. F. Haase, A. Celi, A. Kan, A. Jena, C. Kokail, R. van Bijnen, K. Jansen, P. Zoller, and C. A. Muschik, Simulating 2D effects in lattice gauge theories on a quantum computer, PRX Quantum **2**, 030334 (2021).

[55] T. Angelides, P. Naredi, A. Crippa, K. Jansen, S. Kühn, I. Tavernelli, and D. S. Wang, First-order phase transition of the Schwinger model with a quantum computer, arXiv:2312.12831.

[56] Y. Chai, A. Crippa, K. Jansen, S. Kühn, V. R. Pascuzzi, F. Tacchino, and I. Tavernelli, Entanglement production from scattering of fermionic wave packets: A quantum computing approach, arXiv:2312.02272.

[57] Z. Davoudi, C.-C. Hsieh, and S. V. Kadam, Scattering wave packets of hadrons in gauge theories: Preparation on a quantum computer, arXiv:2402.00840.

[58] R. C. Farrell, M. Illa, A. N. Ciavarella, and M. J. Savage, Scalable circuits for preparing ground states on digital quantum computers: The Schwinger model vacuum on 100 qubits, PRX Quantum **5**, 020315 (2024).

[59] A. Ciavarella, N. Klco, and M. J. Savage, Trailhead for quantum simulation of SU(3) Yang-Mills lattice gauge theory in the local multiplet basis, Phys. Rev. D **103**, 094501 (2021).

[60] R. C. Farrell, I. A. Chernyshev, S. J. M. Powell, N. A. Zemlevskiy, M. Illa, and M. J. Savage, Preparations for quantum simulations of quantum chromodynamics in $1 + 1$ dimensions. II. Single-baryon β-decay in real time, Phys. Rev. D **107**, 054513 (2023).

[61] R. C. Farrell, I. A. Chernyshev, S. J. M. Powell, N. A. Zemlevskiy, M. Illa, and M. J. Savage, Preparations for quantum simulations of quantum chromodynamics in $1 + 1$ dimensions. I. Axial gauge, Phys. Rev. D **107**, 054512 (2023).

[62] Y. Y. Atas, J. F. Haase, J. Zhang, V. Wei, S. M.-L. Pfaendler, R. Lewis, and C. A. Muschik, Simulating one-dimensional quantum chromodynamics on a quantum computer: Real-time evolutions of tetra- and pentaquarks, Phys. Rev. Res. **5**, 033184 (2023).

[63] A. N. Ciavarella, Quantum simulation of lattice QCD with improved Hamiltonians, Phys. Rev. D **108**, 094513 (2023).

[64] A. N. Ciavarella and C. W. Bauer, Quantum simulation of SU(3) lattice Yang Mills theory at leading order in large N, arXiv:2402.10265.

[65] A. Kruckenhauser, R. van Bijnen, T. V. Zache, M. Di Liberto, and P. Zoller, High-dimensional SO(4)-symmetric Rydberg manifolds for quantum simulation, Quantum Sci. Technol. **8**, 015020 (2022).

[66] S. R. Cohen and J. D. Thompson, Quantum computing with circular Rydberg atoms, PRX Quantum **2**, 030322 (2021).

[67] Y. Chi, J. Huang, Z. Zhang, J. Mao, Z. Zhou, X. Chen, C. Zhai, J. Bao, T. Dai, H. Yuan *et al.*, A programmable qudit-based quantum processor, Nat. Commun. **13**, 1166 (2022).

[68] V. Kasper, D. González-Cuadra, A. Hegde, A. Xia, A. Dauphin, F. Huber, E. Tiemann, M. Lewenstein, F. Jendrzejewski, and P. Hauke, Universal quantum computation and quantum error correction with ultracold atomic mixtures, Quantum Sci. Technol. **7**, 015008 (2021).

[69] M. Ringbauer, M. Meth, L. Postler, R. Stricker, R. Blatt, P. Schindler, and T. Monz, A universal qudit quantum processor with trapped ions, Nat. Phys. **18**, 1053 (2022).

[70] P. J. Low, B. White, and C. Senko, Control and readout of a 13-level trapped ion qudit, arXiv:2306.03340.

[71] D. González-Cuadra, T. V. Zache, J. Carrasco, B. Kraus, and P. Zoller, Hardware efficient quantum simulation of non-Abelian gauge theories with qudits on Rydberg platforms, Phys. Rev. Lett. **129**, 160501 (2022).

[72] T. V. Zache, D. González-Cuadra, and P. Zoller, Fermion-qudit quantum processors for simulating lattice gauge theories with matter, Quantum **7**, 1140 (2023).

[73] P. P. Popov, M. Meth, M. Lewestein, P. Hauke, M. Ringbauer, E. Zohar, and V. Kasper, Variational quantum simulation of U(1) lattice gauge theories with qudit systems, Phys. Rev. Res. **6**, 013202 (2024).

[74] M. Meth, J. F. Haase, J. Zhang, C. Edmunds, L. Postler, A. Steiner, A. J. Jena, L. Dellantonio, R. Blatt, P. Zoller, T. Monz, P. Schindler, C. Muschik, and M. Ringbauer, Simulating 2D lattice gauge theories on a qudit quantum computer, arXiv:2310.12110.

[75] I. V. Zalivako, A. S. Nikolaeva, A. S. Borisenko, A. E. Korolkov, P. L. Sidorov, K. P. Galstyan, N. V. Semenin, V. N. Smirnov, M. A. Aksenov, K. M. Makushin *et al.*, Towards multiqudit quantum processor based on a ^{171}Yb$^+$ ion string: Realizing basic quantum algorithms, arXiv:2402.03121.

[76] C. Xu and A. W. Ludwig, Topological quantum liquids with quaternion non-Abelian statistics, Phys. Rev. Lett. **108**, 047202 (2012).

[77] M. Kalinowski, N. Maskara, and M. D. Lukin, Non-Abelian Floquet spin liquids in a digital Rydberg simulator, Phys. Rev. X **13**, 031008 (2023).

[78] D. González-Cuadra, D. Bluvstein, M. Kalinowski, R. Kaubruegger, N. Maskara, P. Naldesi, T. V. Zache, A. M. Kaufman, M. D. Lukin, H. Pichler *et al.*, Fermionic quantum processing with programmable neutral atom arrays, Proc. Natl. Acad. Sci. **120**, e2304294120 (2023).

[79] P. J. Low, B. M. White, A. A. Cox, M. L. Day, and C. Senko, Practical trapped-ion protocols for universal qudit-based quantum computing, Phys. Rev. Res. **2**, 033128 (2020).

[80] L. Susskind, Lattice fermions, Phys. Rev. D **16**, 3031 (1977).

[81] E. Zohar and M. Burrello, Formulation of lattice gauge theories for quantum simulations, Phys. Rev. D **91**, 054506 (2015).

[82] S. Chandrasekharan and U.-J. Wiese, Quantum link models: A discrete approach to gauge theories, Nucl. Phys. B **492**, 455 (1997).

[83] P. Silvi, Y. Sauer, F. Tschirsich, and S. Montangero, Tensor network simulation of an SU(3) lattice gauge theory in 1D, Phys. Rev. D **100**, 074512 (2019).

[84] E. Zohar and J. I. Cirac, Removing staggered fermionic matter in $U(N)$ and $SU(N)$ lattice gauge theories, Phys. Rev. D **99**, 114511 (2019).

[85] K. Mølmer and A. Sørensen, Multiparticle entanglement of hot trapped ions, Phys. Rev. Lett. **82**, 1835 (1999).

[86] C. Roos, T. Zeiger, H. Rohde, H. C. Nägerl, J. Eschner, D. Leibfried, F. Schmidt-Kaler, and R. Blatt, Quantum state engineering on an optical transition and decoherence in a Paul trap, Phys. Rev. Lett. **83**, 4713 (1999).

[87] P. Schindler, D. Nigg, T. Monz, J. T. Barreiro, E. Martinez, S. X. Wang, S. Quint, M. F. Brandl, V. Nebendahl, C. F. Roos, M. Chwalla, M. Hennrich, and R. Blatt, A quantum information processor with trapped ions, New J. Phys. **15**, 123012 (2013).

[88] H. Häffner, S. Gulde, M. Riebe, G. Lancaster, C. Becher, J. Eschner, F. Schmidt-Kaler, and R. Blatt, Precision measurement and compensation of optical Stark shifts for an ion-trap quantum processor, Phys. Rev. Lett. **90**, 143602 (2003).

[89] G. Kirchmair, J. Benhelm, F. Zähringer, R. Gerritsma, C. F. Roos, and R. Blatt, Deterministic entanglement of ions in thermal states of motion, New J. Phys. **11**, 023002 (2009).

[90] T. Ruster, C. T. Schmiegelow, H. Kaufmann, C. Warschburger, F. Schmidt-Kaler, and U. G. Poschinger, A long-lived Zeeman trapped-ion qubit, Appl. Phys. B **122**, 254 (2016).

[91] L. Viola, E. Knill, and S. Lloyd, Dynamical decoupling of open quantum systems, Phys. Rev. Lett. **82**, 2417 (1999).

[92] L. Pelzer, K. Dietze, V. J. Martínez-Lahuerta, L. Krinner, J. Kramer, F. Dawel, N. C. Spethmann, K. Hammerer, and P. O. Schmidt, Multi-ion frequency reference using dynamical decoupling, Phys. Rev. Lett. **133**, 033203 (2024).

[93] I. V. Zalivako, A. S. Borisenko, I. A. Semerikov, A. E. Korolkov, P. L. Sidorov, K. P. Galstyan, N. V. Semenin, V. N. Smirnov, M. D. Aksenov, A. K. Fedorov *et al.*, Continuous dynamical decoupling of optical ^{171}Yb$^+$ qudits with radiofrequency fields, Front. Quantum Sci. Technol. **2**, 1228208 (2023).

[94] S. A. E. A. Moses, A race-track trapped-ion quantum processor, Phys. Rev. X **13**, 041052 (2023).

[95] L. Gerster, F. Martínez-García, P. Hrmo, M. W. van Mourik, B. Wilhelm, D. Vodola, M. Müller, R. Blatt, P. Schindler, and T. Monz, Experimental Bayesian calibration of trapped-ion entangling operations, PRX Quantum **3**, 020350 (2022).

[96] N. Klco, M. J. Savage, and J. R. Stryker, SU(2) non-Abelian gauge field theory in one dimension on digital quantum computers, Phys. Rev. D **101**, 074512 (2020).

[97] H. Liu, T. Bhattacharya, S. Chandrasekharan, and R. Gupta, Phases of 2D massless QCD with qubit regularization, arXiv:2312.17734.

[98] I. D Andrea, C. W. Bauer, D. M. Grabowska, and M. Freytsis, New basis for Hamiltonian SU(2) simulations, Phys. Rev. D **109**, 074501 (2024).

[99] S. V. Mathis, G. Mazzola, and I. Tavernelli, Toward scalable simulations of lattice gauge theories on quantum computers, Phys. Rev. D **102**, 094501 (2020).

[100] O. Katz, L. Feng, A. Risinger, C. Monroe, and M. Cetina, Demonstration of three- and four-body interactions between trapped-ion spins, Nat. Phys. **19**, 1452 (2023).

[101] O. Katz and C. Monroe, Programmable quantum simulations of bosonic systems with trapped ions, Phys. Rev. Lett. **131**, 033604 (2023).

[102] J. Benhelm, G. Kirchmair, C. Roos, and R. Blatt, Experimental quantum-information processing with ^{43}Ca$^+$ ions, Phys. Rev. A **77**, 062306 (2008).

[103] M. Fishman, S. R. White, and E. M. Stoudenmire, The ITensor software library for tensor network calculations, SciPost Phys. Codebases, 4 (2022).

[104] M. Fishman, S. R. White, and E. M. Stoudenmire, Codebase release 0.3 for ITensor, SciPost Phys. Codebases, 4 (2022).